



Numerical Modeling of Galactic Cosmic-Ray Proton and Helium Observed by AMS-02 during the Solar Maximum of Solar Cycle 24

Claudio Corti¹ , Marius S. Potgieter² , Veronica Bindi¹ , Cristina Consolandi¹ , Christopher Light¹ ,
Matteo Palermo¹ , and Alexis Popkow¹

¹ Physics and Astronomy Department, University of Hawaii at Manoa, 2505 Correa Road, Honolulu, HI 96822, USA; corti@hawaii.edu

² Center for Space Research, North-West University, Potchefstroom, 2520, South Africa

Received 2018 October 22; revised 2018 December 20; accepted 2018 December 21; published 2019 February 5

Abstract

Galactic cosmic rays (GCRs) are affected by solar modulation while they propagate through the heliosphere. The study of the time variation of GCR spectra observed at Earth can shed light on the underlying physical processes, specifically diffusion and particle drifts. Recently, the AMS-02 experiment measured with very high accuracy the time variation of the cosmic-ray proton and helium flux between 2011 May and 2017 May in the rigidity range from 1 to 60 GV. In this work, a comprehensive three-dimensional steady-state numerical model is used to solve Parker's transport equation and reproduce the monthly proton fluxes observed by AMS-02. We find that the rigidity slope of the perpendicular mean free path above 4 GV remains constant, while below 4 GV, it increases during solar maximum. Assuming the same mean free paths for helium and protons, the models are able to reproduce the time behavior of the p/He ratio observed by AMS-02. The dependence of the diffusion tensor on the particle mass-to-charge ratio, A/Z , is found to be the main cause of the time dependence of p/He below 3 GV.

Key words: astroparticle physics – cosmic rays – methods: numerical – Sun: activity – Sun: heliosphere

1. Introduction

Galactic cosmic rays (GCRs) are charged particles produced by some of the most energetic phenomena in the universe that travel the endless voids of our galaxy before finally arriving at the edge of the solar system (Amato & Blasi 2017). Here they meet with the heliosphere, a huge cavity carved out of interstellar space by a supersonic stream of magnetized plasma constantly blown out from the Sun called the solar wind (Parker 1958). By the time the GCRs reach Earth, they have interacted with the turbulent magnetic field embedded in the time-varying solar wind: the overall effect of the physical processes involved in this interaction is called solar modulation (Parker 1965; Potgieter 2013a).

In recent years, a new interest in GCRs has been spurred by the observations of an excess in their antimatter components, like positrons (Adriani et al. 2013a; Accardo et al. 2014) and antiprotons (Adriani et al. 2010; Aguilar et al. 2016a), suggesting an exotic origin, such as dark matter annihilation or decay (Turner & Wilczek 1990; Donato et al. 2009) or new astrophysical phenomena (Blasi & Serpico 2009; Hooper et al. 2009; Blum et al. 2013). Since the fluxes of the various species of GCRs are distorted by the influence of the Sun below a few tens of GV, a better understanding of the solar modulation and its time evolution is of paramount importance to correctly deduce their shape before they enter the heliosphere (Fornengo et al. 2013, 2014; Cirelli et al. 2014; Yuan & Bi 2015; Tomassetti 2017).

Since they are a highly ionizing form of radiation that can penetrate the walls of a spacecraft, an astronaut spacesuit, and the human body itself (Cucinotta & Durante 2006), GCRs are also an unavoidable challenge for any human space exploration program. The knowledge of the time variation of the GCR flux and the study of the propagation of particles in the heliosphere will help reduce the uncertainties in the radiation dose predictions (Cucinotta et al. 2013).

Recently, the AMS-02 experiment on board the *International Space Station* measured, with very high accuracy and on the scale of a Bartels rotation (BR; 27 days), the time variation of the cosmic-ray proton and helium flux between 2011 May and 2017 May in the rigidity range from 1 to 60 GV (Aguilar et al. 2018; the data can also be retrieved at NASA's CDAWeb³). The key points of the AMS-02 observations are the complex time behavior due to the short-term activity and the decrease of the p/He ratio coinciding with the start of the flux recovery after the solar maximum.

In this work, we use a comprehensive three-dimensional (3D) numerical model to solve the propagation equation of GCRs in the heliosphere in order to understand the physical processes underlying the AMS-02 results. In the following sections, the numerical model will be detailed, specifying the various ingredients needed to correctly describe the physics of the heliospheric transport of GCRs. Then, the method to reproduce the proton monthly fluxes will be presented, together with the results. Next, the p/He prediction from the best-fit models will be compared with the data, and finally, we will perform a dedicated study to understand the origin of the p/He time dependence.

2. Numerical Model Description

A state-of-the-art 3D steady-state numerical model has been developed during recent years (Potgieter et al. 2014; Vos & Potgieter 2015) to solve the Parker equation of GCR transport in the heliosphere (Parker 1965),

$$\frac{\partial f}{\partial t} + \mathbf{V}_{\text{sw}} \cdot \nabla f - \nabla \cdot (\mathbf{K} \nabla f) - \frac{\nabla \cdot \mathbf{V}_{\text{sw}} R}{3} \frac{\partial f}{\partial R} = 0, \quad (1)$$

where $f(\mathbf{r}, R)$ is the omnidirectional GCR distribution function, \mathbf{V}_{sw} is the solar wind speed, and \mathbf{K} is the diffusion tensor, which

³ https://spdf.gsfc.nasa.gov/pub/data/international_space_station_iss/ams-02/

can be separated into a symmetric part, describing the scattering of particles on the heliospheric magnetic field (HMF) irregularities, and an asymmetric part, describing particle drifts along magnetic field gradients, curvatures, and the heliospheric current sheet (HCS). In the steady-state approximation, $\partial f/\partial t = 0$; this is a reasonable assumption during the solar minimum but less so during the solar maximum. Nevertheless, for studies of the time variation of GCR fluxes averaged over BRs, it is still acceptable.

The model uses a finite-difference solver, the alternating-direction implicit method (Peaceman & Rachford 1955), to obtain f at all positions in the heliosphere. This method has been adapted to cope with four numerical dimensions: three spatial (therefore called 3D) and one to handle rigidity. Including a time dependence would make the method numerically unsuitable, so either one spatial dimension should be sacrificed (Ngobeni & Potgieter 2014) or the so-called stochastic differential equation approach should be followed (see, e.g., Kopp et al. 2017; Luo et al. 2017 and references therein).

2.1. Solar Wind, HMF, and Current Sheet

The solar wind velocity profile is assumed to be separable in a radial and latitudinal component:

$$\mathbf{V}_{\text{sw}}(r, \theta) = V_r(r) V_\theta(\theta) \hat{\mathbf{r}}. \quad (2)$$

The radial component describes the fast rise to supersonic speed within the first 0.3 au from the Sun (first term of Equation (3)) and the transition to subsonic speed at the termination shock (second term of Equation (3)),

$$V_r(r) = 1 - \exp\left[\frac{40}{3}\left(\frac{r_\odot - r}{r_0}\right)\right] + \left[\frac{s+1}{2s} - \frac{s-1}{2s} \tanh\left(\frac{r - r_{\text{TS}}}{L}\right) - 1\right], \quad (3)$$

where $r_\odot = 0.005$ au is the Sun radius, $r_0 = 1$ au, r_{TS} is the radial position of the termination shock (which, in principle, can vary in time), $L = 1.2$ au is the width of the shock barrier, and $s = 2.5$ is the shock compression ratio in the downstream region, i.e., the ratio of the velocity before and after the shock.

The latitudinal term describes the transition between the slow (polar) and fast (equatorial) component of the solar wind,

$$V_\theta(\theta) = \frac{V_{\text{pol}} + V_{\text{eq}}}{2} \mp \frac{V_{\text{pol}} - V_{\text{eq}}}{2} \tanh[6.8(\theta' \pm \xi)], \quad (4)$$

where V_{pol} and V_{eq} are, respectively, the polar and equatorial solar wind speed components; $\theta' = \theta - \pi/2$; and ξ is the polar angle at which the transition between the equatorial and polar streams begins. The top and bottom signs correspond, respectively, to the northern ($0 < \theta < \pi/2$) and southern ($\pi/2 < \theta < \pi$) hemisphere. During periods of solar maximum, there is no clear latitudinal dependence of the solar wind speed, so that on average, $V_{\text{pol}} = V_{\text{eq}}$, and the second term of Equation (4) vanishes.

The reacceleration at the termination shock via diffusive shock acceleration is not included in the model, since for protons above 1 GV, the effects of the termination shock at Earth are negligible (see, e.g., Langner & Potgieter 2005 and references therein). The drop in solar wind velocity at the

termination shock is taken into account in the evaluation of the HMF and diffusion tensor, reproducing the actual diffusion barrier present at the shock.

The HMF implemented in this model is the Parker field with the Smith–Bieber modification,

$$\mathbf{B}(r, \theta, \phi) = B_n \left(\frac{r}{r_0}\right)^2 (\hat{\mathbf{r}} - \tan \psi \hat{\boldsymbol{\phi}}) \times [1 - 2H(\theta - \theta_{\text{HCS}})], \quad (5)$$

where B_n is a normalization factor dependent on the observed magnitude of the HMF at Earth, B_0 ; H is the Heaviside step function, which describes the opposite polarity above and below the HCS; θ_{HCS} is the polar position of the HCS; and ψ is the spiral angle, i.e., the angle between the direction of the HMF and the radial direction. Here ψ is defined as

$$\tan \psi = \frac{\Omega(r - b) \sin \theta}{V_{\text{sw}}(r, \theta)} - \frac{r V_{\text{sw}}(b, \theta) B_T(b)}{b V_{\text{sw}}(r, \theta) B_R(b)}, \quad (6)$$

where Ω is the angular rotation frequency of the Sun, $b = 20 r_\odot$ is the distance from the Sun where the HMF becomes fully radial, and $B_T(b)/B_R(b) \approx -0.02$ is the ratio of the azimuthal-to-radial magnetic field components (Smith & Bieber 1991). Imposing $B(r_0, \pi/2) = B_0$, we obtain $B_n = B_0/\sqrt{1 + \tan^2 \psi(r_0, \pi/2)}$. See also Raath et al. (2016) for a detailed study of the Smith–Bieber and other HMF modifications.

The position of the HCS is given by Kóta and Jokipii (1983),

$$\theta_{\text{HCS}} = \frac{\pi}{2} - \tan^{-1} \left[\tan \alpha \sin \left(\phi + \Omega \frac{r - r_\odot}{V_{\text{sw}}(r, \theta)} \right) \right], \quad (7)$$

where α is the tilt angle, i.e., the maximum latitudinal extent of the HCS. To avoid numerical instabilities created by the discontinuity of the polarity flip when passing from one side of the HCS to the other, the Heaviside function is replaced with a smooth transition function,

$$A \tanh \left(0.549 \frac{\theta_{\text{HCS}} - \theta}{\Delta \theta_{\text{HCS}}} \right), \quad (8)$$

where A is the HMF polarity (± 1) and $\Delta \theta_{\text{HCS}} = 2R_L/r = 2R/(rBc)$ is the angle spanned by two gyroradii for a particle with rigidity R . This means that the HCS drift effects are taken into account only if the particle is within 2 gyroradii from the HCS. See also Raath et al. (2015) for a detailed study of how the treatment of the HCS in numerical modeling studies affects cosmic-ray modulation.

2.2. Diffusion and Drift Coefficients

The rigidity dependence of the parallel diffusion coefficient is approximated by a double power law with a smooth change of slope, while the radial dependence is assumed to be inversely proportional to the magnitude of the HMF:

$$k_{\parallel} = k_{\parallel}^0 \beta \frac{1 \text{ nT}}{B} \left(\frac{R}{R_k}\right)^a \left[1 + \left(\frac{R}{R_k}\right)^s \right]^{\frac{b-a}{s}}, \quad (9)$$

where k_{\parallel}^0 is a normalization factor; $\beta = v/c$; R_k is the rigidity at which the transition between the two power laws happens;

a and b are, respectively, the slopes of the low- and high-rigidity power laws; and s controls the smoothness of the transition. The perpendicular diffusion coefficients are assumed to be proportional to the parallel diffusion coefficient,

$$k_{\perp,r} = k_{\perp,r}^0 k_{\parallel}, \quad k_{\perp,\theta} = u(\theta) k_{\perp,\theta}^0 k_{\parallel}, \quad (10)$$

where $k_{\perp,r}^0$ and $k_{\perp,\theta}^0$ are scaling factors of the order of percent, while $u(\theta)$ is a function that enhances the perpendicular diffusion in the polar regions and is defined as

$$u(\theta) = \frac{3}{2} + \frac{1}{2} \tanh \left[8 \left(\left| \theta - \frac{\pi}{2} \right| - 35^\circ \right) \right]. \quad (11)$$

The numerical values are chosen to reproduce cosmic-ray observations at higher latitudes by the *Ulysses* spacecraft (Potgieter & Haasbroek 1993; Kóta & Jokipii 1995; Potgieter 2000; Heber & Potgieter 2006; Potgieter 2013b). We note that forcing on $k_{\perp,r}$ and $k_{\perp,\theta}$ the same rigidity dependence of k_{\parallel} is a simplification, since both turbulence theory and observations predict a different rigidity behavior (see, e.g., Burger et al. 2000 and references therein). In this work, the slopes of the perpendicular diffusion coefficient are not constrained to be equal to those of the parallel diffusion coefficient; therefore, we introduce the parameters a_{\parallel} , b_{\parallel} (slopes of the parallel diffusion coefficient) and a_{\perp} , b_{\perp} (slopes of the perpendicular diffusion coefficient). The transition rigidity R_k and the smoothness factor s are instead assumed to be the same for all diffusion coefficients; for an overview of these aspects, see Potgieter (2017).

The drift coefficient is defined as

$$k_A = k_A^0 \frac{\beta R}{3B} \frac{(R/R_A)^2}{1 + (R/R_A)^2}, \quad (12)$$

where k_A^0 is a normalization factor that can be used to reduce the overall drift effects, while R_A is the rigidity below which the drift is suppressed due to scattering. For a detailed study of how this expression is obtained and what effects it has on solar modulation of GCRs, see Ngobeni & Potgieter (2015) and Ndanganeni & Potgieter (2016). This approach means that the model is diffusion-dominated, rather than drift-dominated as the original drift models of the 1980s and 1990s were and also as recently applied by, e.g., Tomassetti et al. (2017).

2.3. Local Interstellar Spectrum

The proton and helium local interstellar spectrum (LIS) are parameterized between 0.1 GV and 3 TV as a combination of four smooth power laws in rigidity,

$$\frac{dJ_{\text{LIS}}}{dR} = N \left(\frac{R}{1 \text{ GV}} \right)^{\gamma_0} \prod_{i=1}^3 \left[\frac{1 + (R/R_i)^{s_i}}{1 + R_i^{-s_i}} \right]^{\Delta_i/s_i}, \quad (13)$$

where N is the flux normalization at 1 GV, γ_0 is the spectral index of the first power law, $\Delta_i = \gamma_i - \gamma_{i-1}$ is the difference in spectral index between the i th power law and the previous one, R_i are the rigidities at which the breaks between power laws happen, and s_i controls the smoothness of the breaks.

Following the same method as in Corti et al. (2016), the proton LIS is derived by a combined fit on low-rigidity data measured by *Voyager 1* outside the heliosphere (Stone et al. 2013) and

high-rigidity data measured by AMS-02 (Aguilar et al. 2015), modulated with the force-field approximation (Gleeson & Axford 1968). The best-fit parameters are $N = (5658 \pm 57)/(\text{m}^2 \text{ sr s GV})$, $\gamma_0 = 1.669 \pm 0.005$, $R_1 = (0.572 \pm 0.004) \text{ GV}$, $\Delta_1 = -4.117 \pm 0.005$, $s_1 = 1.78 \pm 0.02$, $R_2 = (6.2 \pm 0.2) \text{ GV}$, $\Delta_2 = -0.423 \pm 0.008$, $s_2 = 3.89 \pm 0.49$, $R_3 = (540 \pm 240) \text{ GV}$, $\Delta_3 = -0.26 \pm 0.1$, and $s_3 = 1.53 \pm 0.43$. This LIS is consistent within 0.2% with the one from Corti et al. (2016).

The ^3He and ^4He LISs are derived by a combined fit to multiple data sets⁴: *Voyager 1* He (Cummings et al. 2016), *Voyager 1* ^3He and ^4He (Webber et al. 2018), IMAX $^3\text{He}/^4\text{He}$ (Reimer et al. 1998), BESS ^3He and ^4He (Wang et al. 2002; Myers et al. 2003), AMS-01 ^3He and ^4He (Aguilar et al. 2011), PAMELA ^3He and ^4He (Adriani et al. 2016), and AMS-02 He (Aguilar et al. 2017). The *Voyager 1* data were measured outside the heliosphere, while all other data were collected at 1 au at different solar activity conditions, so they were modulated with the force-field approximation. We allowed the modulation parameter for ^3He to be different from the modulation parameter for ^4He (see Section 5 for the dependence of the results on this assumption). According to the standard model of GCR production, acceleration, and transport in the galaxy, ^4He is produced in astrophysical sources, while ^3He is produced by collisions of heavier nuclei with the interstellar material, so that $^3\text{He}/^4\text{He}$ at very high rigidity ($\gtrsim 100 \text{ GV}$) becomes proportional to $1/D$, where $D \propto R^\delta$ is the diffusion coefficient in the galaxy (Amato & Blasi 2017). The latest B/C data from AMS-02 (Aguilar et al. 2016b) constrain δ to be $-1/3$, in agreement with Kolmogorov's theory of interstellar turbulence (Kolmogorov 1941). Furthermore, at high rigidities, propagation in the galaxy should be mostly dependent on rigidity only, while at low rigidity, energy-loss processes are also velocity-dependent. For these reasons, the parameters R_2 , s_2 , R_3 , Δ_3 , and s_3 for ^3He are assumed to be equal to the ones for ^4He , while $\gamma_2(^3\text{He}) = \gamma_2(^4\text{He}) - 1/3$. The parameters N , γ_0 , R_1 , Δ_1 , and s_1 are instead left free independently for ^3He and ^4He . The best-fit parameters for ^4He are $N = (362 \pm 4)/(\text{m}^2 \text{ sr s GV})$, $\gamma_0 = 2.113 \pm 0.007$, $R_1 = (1.15 \pm 0.01) \text{ GV}$, $\Delta_1 = -5.79 \pm 0.01$, $s_1 = 1.27 \pm 0.01$, $R_2 = (5.2 \pm 0.5) \text{ GV}$, $\Delta_2 = 0.47 \pm 0.01$, $s_2 = 2.19 \pm 0.06$, $R_3 = (298 \pm 38) \text{ GV}$, $\Delta_3 = 1.063 \pm 0.003$, and $s_3 = 0.270 \pm 0.008$. The best-fit parameters for ^3He are $N = (60.2 \pm 1.5)/(\text{m}^2 \text{ sr s GV})$, $\gamma_0 = 2.29 \pm 0.04$, $R_1 = (2.37 \pm 0.08) \text{ GV}$, and $\Delta_1 = -10 \pm 0.9$, $s_1 = 1.27 \pm 0.06$.

Figure 1 shows a comparison of the p, ^3He , ^4He , and He (equal to $^3\text{He} + ^4\text{He}$) LIS parameterizations (top panel) and their ratios (bottom panel). For alternative methods of obtaining the proton and helium LISs, see Bisschoff & Potgieter (2016), and for a discussion of the impact of the *Voyager* and PAMELA observations on determining the appropriate LIS, see Potgieter (2014).

3. Reproduction and Fit of the AMS-02 Monthly Proton Fluxes

The standard approach of a least-squares fit with MINUIT (James & Roos 1975) is not feasible in this work, since a single model runs too slowly to allow the thousands of sequential iterations needed to find a global minimum. Furthermore, the fit should be repeated for each of the 79 BRs observed by

⁴ IMAX, BESS, AMS-01, and PAMELA data have been downloaded from the CRDB (Maurin et al. 2014): <https://lpsc.in2p3.fr/cosmic-rays-db>.

Table 1
Definition of the Grid of Input Parameters Used to Generate the Numerical Models

Parameter	Symbol	Values
HMF polarity	A	$< 0, > 0$
Tilt angle (deg)	α	20, 25, 30, 35, 40, 55, 65, 75
HMF magnitude at Earth (nT)	B_0	4.5, 5.5, 6.0, 6.5, 7.5, 8.5
Normalization of the parallel diffusion coefficient ($6 \times 10^{20} \text{ cm}^2 \text{ s}^{-1}$)	k_{\parallel}^0	50, 70, 90, 110, 130, 150, 170, 190, 210, 230 ^a , 250 ^a
Low-rigidity slope of the parallel diffusion coefficient	a_{\parallel}	0.2, 0.5, 0.8, 1.1, 1.4, 1.7, 2.0
High-rigidity slope of the parallel diffusion coefficient	b_{\parallel}	0.2, 0.5, 0.8, 1.1, 1.4, 1.7, 2.0, 2.3
Low-rigidity slope of the perpendicular diffusion coefficient	a_{\perp}	0.2, 0.5, 0.8, 1.1, 1.4, 1.7, 2.0
High-rigidity slope of the perpendicular diffusion coefficient	b_{\perp}	0.2, 0.5, 0.8, 1.1, 1.4, 1.7, 2.0, 2.3

Note.

^a Only for $A > 0$ models.

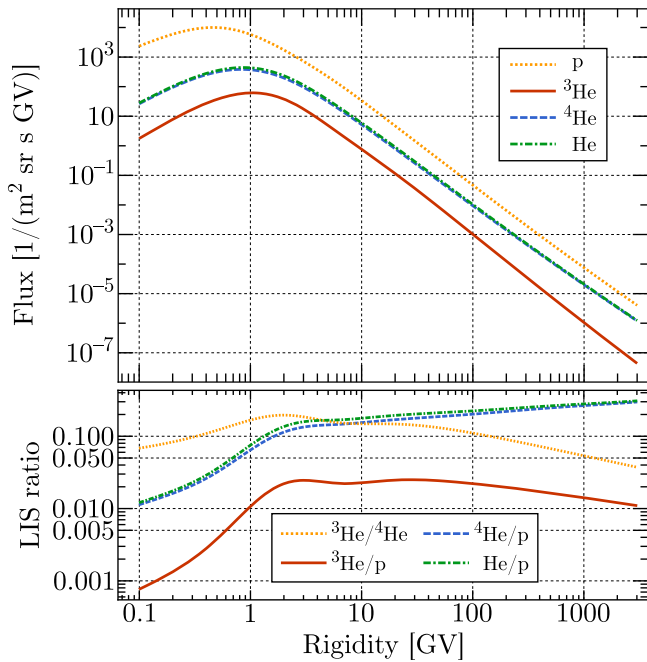


Figure 1. Top: the p (dotted yellow), ${}^3\text{He}$ (solid red), ${}^4\text{He}$ (dashed blue), and He (dotted-dashed green) LIS parameterizations used in this paper, derived by a combined fit to *Voyager 1* unmodulated data and various modulated data sets collected at 1 au at different times (see text for details). Bottom: the ${}^3\text{He}/{}^4\text{He}$ (dotted yellow), ${}^3\text{He}/\text{p}$ (solid red), ${}^4\text{He}/\text{p}$ (dashed blue), and He/p (dotted-dashed green) LIS ratio.

AMS-02, potentially generating a given model multiple times and thus wasting computing time. To solve this issue, a different strategy has been developed.

An ensemble of models is created in parallel, each with a different combination of input parameters. The resulting multidimensional grid of models is linearly interpolated to find the set of parameters that minimizes the χ^2 between the models and the data. This way, the models are generated only once, and they can be reused in the fitting of every flux, avoiding their duplication. The parameters and their values defining the multidimensional grid are listed in Table 1.

The normalization of the perpendicular radial and polar diffusion coefficients has been kept fixed at $k_{\perp,r}^0 = 0.02$ and $k_{\perp,\theta}^0 = 0.01$, consistent with the values found by Zhao et al. (2014), Vos & Potgieter (2015), and Potgieter & Vos (2017) analyzing data from PAMELA and with the expectation of turbulence theory (see, e.g., Burger et al. 2000 and

Bieber et al. 2004). The parameters describing the drift processes, R_A and k_A^0 , are set to the values used for reproducing PAMELA data, i.e., 0.55 GV and 1, respectively. The transition rigidity R_k and the smoothness of the change of slope s are the same for all three diffusion coefficients and equal to 4.3 GV and 2.2, respectively. The termination shock is fixed at 80 au and the heliopause at 122 au, consistent with the *Voyager* observations. The equatorial and fast solar wind components have been assumed to have the same speed, $V_0 = 440 \text{ km s}^{-1}$, since we are mostly analyzing the solar maximum period.

The spatial grid has 609 steps in the radial direction, from 0.4 to 122 au; 145 steps in the polar direction, from 0 to π ; and 33 steps in the longitudinal direction, from 0 to 2π . The rigidity grid has been divided into 245 steps, uniformly distributed in logarithmic space between 1 and 200 GV. To reduce the output file size, the solution has been saved in a reduced spatial grid, with a radial step of 2 au, a latitudinal step of 5° , and at $\phi = 0$. The latter choice is justified by the fact that the modulated flux at Earth is negligibly dependent on the heliographic longitude; indeed, the flux variation around the average value is of the order of 0.3%.

More than 3 million models have been generated, for a running time of 10 weeks and a total disk size of 4.6 TB.

3.1. Heliosphere Status

A steady-state model assumes that the heliosphere status is frozen in the whole time interval during which the particles propagate from the heliopause to Earth. Clearly, this assumption is never valid in a dynamical system like the heliosphere, especially during periods of high solar activity, when the HMF and tilt angle can have large variations on a monthly basis. Nevertheless, the steady-state approximation is widely used, due to the simplicity of the treatment of the numerical solution of the Parker equation (see, e.g., Potgieter et al. 2014; Zhao et al. 2014; and Vos & Potgieter 2015).

As a first approximation, a way to take into account the time-varying status of the heliosphere is to use an average value for α and B_0 . Given a BR, we take the average of the tilt angle and HMF over a time period preceding the selected BR. This time period has been chosen such that the average values of α and B_0 reflect the average conditions sampled by GCRs while propagating from the heliopause to Earth. Since the HMF is frozen in the solar wind, it propagates with the same velocity: if $V_0 = 440 \text{ km s}^{-1}$, taking into account the drop in velocity at the termination shock, the propagation time is of the order of 2 yr. However, GCRs diffuse inward in a much shorter period

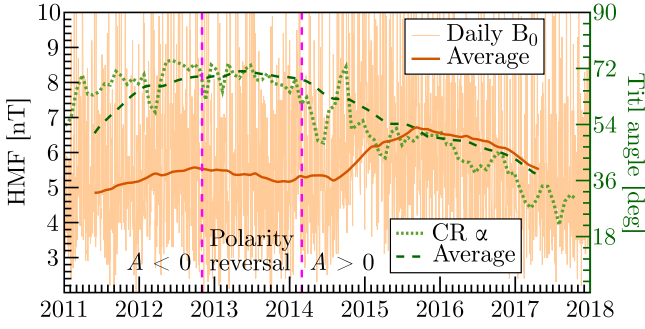


Figure 2. Time variation of the tilt angle, α , measured in Carrington rotations by the WSO (green dotted line) and the daily HMF magnitude, B_0 , obtained by OMNIWeb (thin orange lines). The dashed dark green and solid brown lines are the 1 yr backward average of, respectively, the tilt angle and the HMF for every BR. The vertical dashed magenta lines delimit the period of the solar magnetic field polarity reversal.

of time, between 1 and 4 months (Strauss et al. 2011), and do not spend the same amount of time at all radial distances. In fact, the more they penetrate the heliosphere, the more energy they lose, so that the residing time increases going toward the Sun. At the same time, most of the modulation happens in the heliosheath, as observed by *Voyager 1* (see, e.g., Webber et al. 2012 and Vos & Potgieter 2015). We decided to consider a period of 1 yr, during which the heliosphere conditions affect the GCRs. See Section 4 for a discussion of the dependence of the results on the duration of this period.

Figure 2 illustrates the time variation of the tilt angle, measured every Carrington rotation by the Wilcox Solar Observatory⁵, and the daily HMF observed at 1 au by the *ACE* and *Wind* spacecraft.⁶ The values used as input for the models are computed with a 1 yr backward average and shown with thick lines.

For each BR, the tilt angle and HMF are fixed to the values $\langle\alpha\rangle$ and $\langle B_0\rangle$ obtained by the 1 yr backward average. Since the grid has only a few discrete values of α and B_0 , a 2D linear interpolation is used to obtain the modulated flux $\Phi(\langle\alpha\rangle, \langle B_0\rangle)$ corresponding to the average heliosphere status. Let us define $\Phi_{i,j} = \Phi(\alpha_i, B_{0,j}; \mathbf{Q})$, where $\mathbf{Q} = (k_{\parallel}^0, a_{\parallel}, b_{\parallel}, a_{\perp}, b_{\perp})$ is a vector representing one of the possible combinations of the remaining parameters of the grid, while i and j are the points on, respectively, the α axis and B_0 axis, for which $\alpha_i \leq \langle\alpha\rangle \leq \alpha_{i+1}$ and $B_{0,j} \leq \langle B_0\rangle \leq B_{0,j+1}$. Let us also define the interpolating factors $s_{\alpha} = (\langle\alpha\rangle - \alpha_i) / (\alpha_{i+1} - \alpha_i)$ and $s_{B_0} = (\langle B_0\rangle - B_{0,i}) / (B_{0,i+1} - B_{0,i})$. If $\langle\alpha\rangle$ or $\langle B_0\rangle$ is outside the range covered by the generated grid, then s_{α} and s_{B_0} are computed using the two closest points to $\langle\alpha\rangle$ and $\langle B_0\rangle$. A first interpolation is performed on the B_0 axis: $\Phi_i(\langle B_0\rangle) = (1 - s_{B_0})\Phi_{i,j} + s_{B_0}\Phi_{i,j+1}$ and $\Phi_{i+1}(\langle B_0\rangle) = (1 - s_{B_0})\Phi_{i+1,j} + s_{B_0}\Phi_{i+1,j+1}$. The final interpolation is carried out on the α axis: $\Phi(\langle\alpha\rangle, \langle B_0\rangle) = (1 - s_{\alpha})\Phi_i(\langle B_0\rangle) + s_{\alpha}\Phi_{i+1}(\langle B_0\rangle)$. The procedure is repeated for all of the grid combinations of \mathbf{Q} . We verified in a small subsample of the models that the 2D linear interpolation does not introduce any bias in the fluxes with respect to generating a model directly with $\langle\alpha\rangle$ and $\langle B_0\rangle$; the difference due to the interpolation procedure is always much smaller than 1%.

⁵ We used the classic model (line of sight) from <http://wso.stanford.edu/Tilts.html> (Hoeksema 1995).

⁶ The HMF magnitude data have been downloaded by NASA/GSFC's OMNI data set through OMNIWeb: <https://omniweb.gsfc.nasa.gov/index.html>.

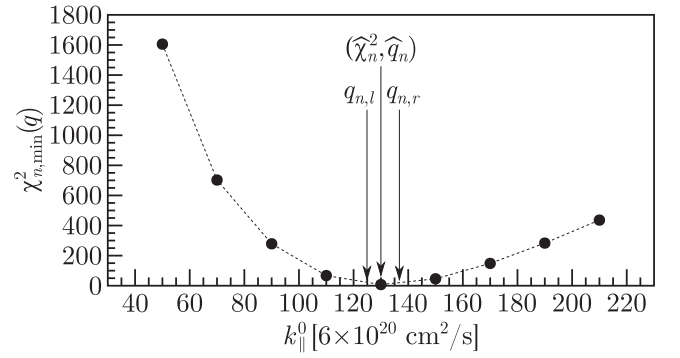


Figure 3. Uncertainty estimation for the normalization of the parallel diffusion coefficient, k_{\parallel}^0 (Equation (9)), in BR 2447. The circles are $\chi_{n,\min}^2(q)$, and the positions of $\hat{\chi}_n^2$, \hat{q}_n , $q_{n,l}$, and $q_{n,r}$ are indicated by arrows. The dashed line is just for guiding the eye.

A good fraction of the monthly fluxes were collected by AMS-02 during the period of the magnetic field polarity reversal. Since the model expects a well-defined polarity, it is not possible to correctly describe the heliosphere status in this time interval. For this reason, both models with negative and positive polarity have been used to describe the BRs between 2013 October and 2015 February, while before 2013 October, the polarity was only negative, and after 2015 February, it was only positive. The reversal period ended in 2014 February, but we decided to extend it up to 1 yr later to take into account the propagation through the heliosphere.

3.2. Best-fit Parameters Estimation

The interpolated fluxes are used to estimate the best-fit parameters k_{\parallel}^0 , a_{\parallel} , b_{\parallel} , a_{\perp} , and b_{\perp} and their time variation. For every BR n and model m (with the corresponding set of parameters \mathbf{Q}_m), the χ^2 , $\chi_{n,m}^2$, between the generated flux $\Phi_{n,m} = \Phi(\langle\alpha\rangle_n, \langle B_0\rangle_n; \mathbf{Q}_m)$ and the flux F_n measured by AMS-02 is computed:

$$\chi_{n,m}^2 = \sum_i \left(\frac{F_{n,i} - \Phi_{n,m}(\tilde{R}_i)}{\sigma_{n,i}} \right)^2, \quad (14)$$

where i is the rigidity binning index of the AMS-02 data, and $\sigma_{n,i}$ is the AMS-02 uncertainty in the i th rigidity bin. The generated flux $\Phi_{n,m}$ is evaluated at the rigidity $\tilde{R}_i = \sqrt{R_i R_{i+1}}$, where R_i and R_{i+1} are the left and right edge of the i th rigidity bin, by interpolating the flux value between consecutive rigidity steps with a power law. The model $\hat{m}(n)$ with the minimum χ^2 , $\hat{\chi}_n^2 = \chi_{n,\hat{m}(n)}^2$, is considered as the best-fit model for the n th BR and the corresponding parameters, $\hat{\mathbf{Q}}_n = \mathbf{Q}_{\hat{m}(n)}$, as the best-fit parameters.

The uncertainty on a given parameter is estimated in the following way. For every value q of the parameter, the minimum χ^2 , $\chi_{n,\min}^2(q)$ is found, regardless of the values of all of the other parameters (i.e., we marginalize over the other parameters); let us note that $\chi_{n,\min}^2(\hat{q}_n) = \hat{\chi}_n^2$, where \hat{q}_n is the best-fit value of the given parameter. We then find the values $q_{n,l}$ and $q_{n,r}$, respectively, to the left and right of \hat{q}_n , for which $\chi_{n,\min}^2(q_{n,l}) = \chi_{n,\min}^2(q_{n,r}) = \hat{\chi}_n^2 + 1$. The lower uncertainty is defined as $\hat{q}_n - q_{n,l}$, while the upper uncertainty is defined as $q_{n,r} - \hat{q}_n$. Figure 3 shows an example of uncertainty estimation for the normalization of the parallel diffusion coefficient, k_{\parallel}^0 , in

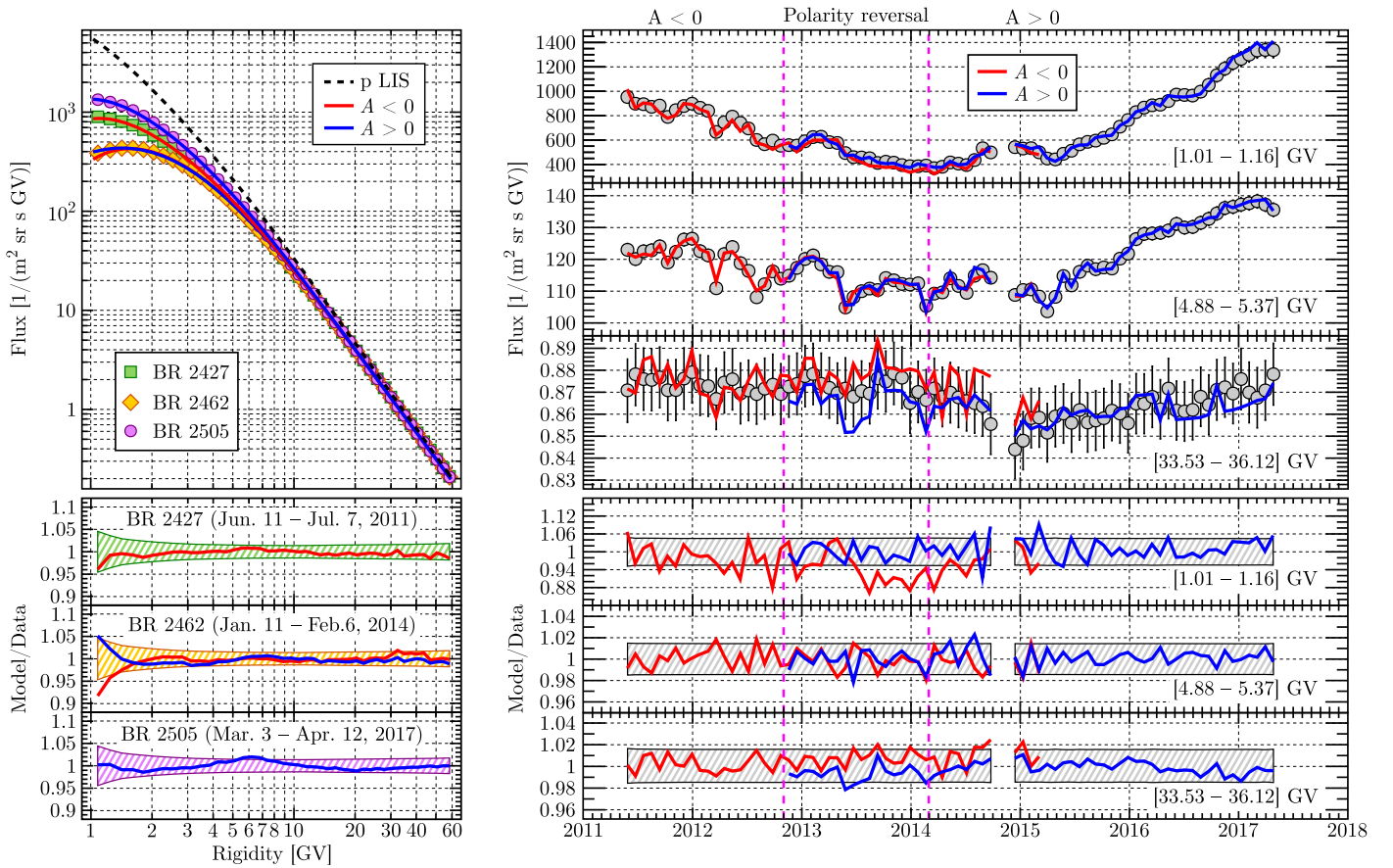


Figure 4. Top left: three selected AMS-02 proton fluxes (colored symbols) as a function of rigidity, together with their best-fit models (red and blue lines) and the proton LIS (dashed black line). Bottom left: ratio of best-fit models to data for the three proton fluxes (red and blue lines), compared to the corresponding AMS-02 uncertainties (colored hatched regions). Top right: three selected rigidity bins of the AMS-02 proton fluxes as a function of time (gray circles), together with their best-fit models (red and blue lines). Bottom right: ratio of best-fit models to data for the three rigidity bins (red and blue lines), compared to the corresponding AMS-02 uncertainties (gray hatched regions). The vertical dashed magenta lines delimit the period of the solar magnetic field polarity reversal.

BR 2447 (2012 December 2–28), with $\hat{\chi}_n^2$, \hat{q}_n , $q_{n,l}$, and $q_{n,r}$ indicated by arrows. The $\chi_{n,\min}^2(q)$ curve is well behaved, being approximately parabolic around the best-fit value.

4. Numerical Results

Figure 4 shows some examples of fitted fluxes. In the top left panel, three AMS-02 proton fluxes at different levels of solar activity are plotted as a function of rigidity: BR 2427 (2011 June 11–July 7) in green squares, corresponding to the ascending phase of solar cycle 24 and a moderate level of solar modulation; BR 2462 (2014 January 11–February 6) in orange diamonds, corresponding to the solar maximum and a very depleted GCR intensity; and BR 2505 (2017 March 3–April 12) in magenta circles, corresponding to the descending phase of solar cycle 24 and a low level of solar modulation. The best-fit models are also shown: BR 2427 was modeled with negative polarity (red line); BR 2462 with both negative (red line) and positive polarity (blue line), since it was during the period of polarity reversal; and BR 2505 with positive polarity (blue line). For reference, the proton LIS is also shown as a dashed black line. In the bottom left panel, the ratio between the best-fit models and data for the three selected fluxes (red and blue lines) is shown and compared to the corresponding uncertainty on the AMS-02 fluxes (colored hatched regions). These plots highlight the very good agreement between the models and data at all rigidities, mostly within the experimental

uncertainties. A similar level of agreement is also obtained for all other fluxes.

In the top right panel of Figure 4, three rigidity bins of the AMS-02 proton fluxes as a function of time have been chosen (gray circles): [1.01–1.16], [4.88–5.37], and [33.53–36.12] GV. The best-fit models are shown as red (negative polarity models) and blue (positive polarity models) lines. As previously mentioned (Section 3.1), both negative and positive polarity models were used in the period from 2013 October to 2015 February. As shown, the time dependence of the proton flux is not exactly the same at different rigidities; for example, after 2013 June, the flux at 5 GV stays almost flat with month-to-month fluctuations, while the flux at 1 GV keeps decreasing until 2014 February. The flux around 35 GV, instead, is mostly constant until the maximum, decreases around 3.5% over the course of 10 months after the polarity reversal, and finally starts to slowly recover (about $2\% \text{ yr}^{-1}$) after 2015 January. All of these rigidity-dependent features in the time variation of the proton fluxes are reproduced by the best-fit models. In the bottom right panel, the ratio between the best-fit models and data for the three selected rigidity bins (red and blue lines) is shown, together with the corresponding uncertainty on the AMS-02 fluxes (gray hatched regions). The models are mostly within the experimental uncertainties at all rigidities.

The values of the best-fit parameters, together with their estimated uncertainties, are listed in Tables 2 and 3 in the Appendix. The time variation of the best-fit parameters is analyzed in Figure 5. In the top panel, the tilt angle (dashed

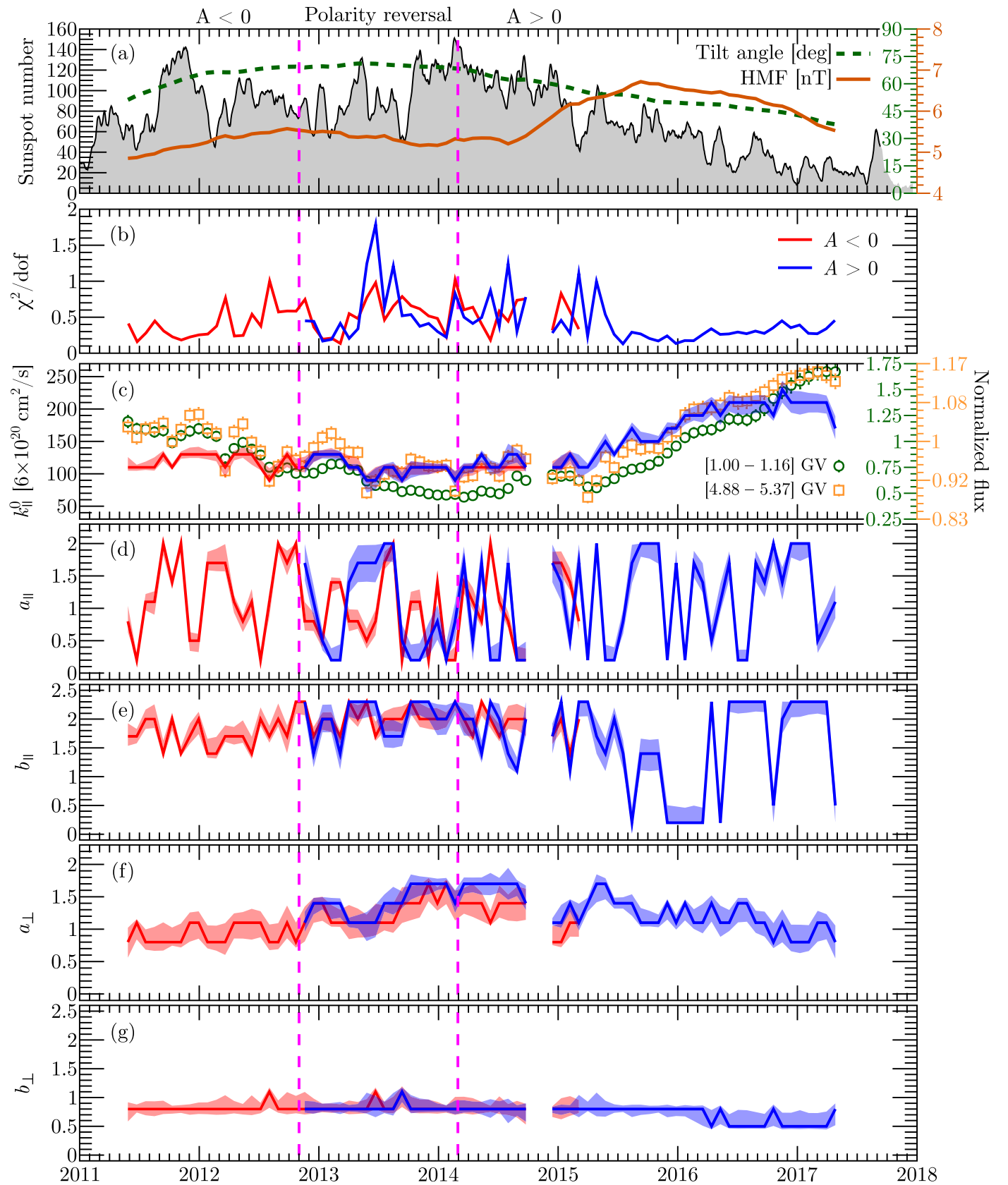


Figure 5. Time variation of the best-fit parameters (lines) and their uncertainties (bands) for models with negative (red) and positive (blue) magnetic polarity. (a) Sunspot number (gray area, 27 day running average), HMF (brown line), and tilt angle (dashed green line) used as input parameters in the models. (b) Normalized χ^2 of the best-fit models. (c) Normalization of the diffusion coefficient, k_{\parallel}^0 , together with two rigidity bins of AMS-02 normalized fluxes (green circles and orange squares). (d) and (e) Low- and high-rigidity slopes of the parallel diffusion coefficient, a_{\parallel} and b_{\parallel} . (f) and (g) Low- and high-rigidity slopes of the perpendicular diffusion coefficient, a_{\perp} and b_{\perp} . The vertical dashed magenta lines delimit the period of the solar magnetic field polarity reversal.

green line, right axis) and HMF (brown line, right axis) used as input in every BR are displayed for reference, together with the daily sunspot number (SILSO World Data Center 2011) smoothed with a 27 day running average (gray area, left axis).

The second panel shows the normalized minimum χ^2 , $\widehat{\chi}_n^2/\text{dof}$, for models with negative (red) and positive (blue) polarity. In general, the agreement between the best-fit models and data is very good for all months, as also shown by the bottom panels of Figure 4. After 2015 August, the normalized χ^2 stays flatter and with fewer fluctuations with respect to the previous months; this is probably due to the fact that in this period, the heliosphere is globally quieter than before, and thus the steady-state approximation used to solve the Parker equation is more valid. The sudden increases of the normalized χ^2 for the positive polarity models in the middle of 2013, during the period of the polarity reversal, might be considered statistical fluctuations but also an indication that modeling a mixed-polarity heliosphere is necessary to correctly describe GCR fluxes during the solar maximum.

The third panel shows the best-fit values (lines) for the normalization of the parallel diffusion coefficient (Equation (9)) with their estimated uncertainties (bands), together with the monthly AMS-02 fluxes in the rigidity bins [1.00–1.16] GV (green circles) and [4.88–5.37] GV (orange squares), normalized to their averaged values. The variations of k_{\parallel}^0 closely follow the time dependence of the observed fluxes (especially around 5 GV), as expected, since k_{\parallel}^0 is the main parameter that controls the level of modulation. For example, the drops of k_{\parallel}^0 (i.e., short-term increases in the modulation strength) correspond with the drops of the proton fluxes, e.g., in 2011 October or 2012 March. A caveat of this analysis is that these drops are due to CMEs hitting the Earth, i.e., local disturbances, which are not included in the model. Nevertheless, the model is able to reproduce the flux by globally changing the diffusion coefficient in order to match the local conditions. We expect that, in these cases, the solution at positions far from Earth will not be accurate, since the diffusion in these positions is not affected by the CME. It is worth noting that, in the period of the polarity reversal, the best-fit k_{\parallel}^0 obtained from models with negative polarity agrees with the one from models with positive polarity; i.e., the normalization of the diffusion coefficient seems to be mostly insensitive to the sign of the HMF polarity. We computed the Pearson correlation between k_{\parallel}^0 and the proton flux intensity at different rigidities, taking into account the uncertainties on the measured fluxes and best-fit values with a toy Monte Carlo. The maximum correlation $r = 0.82$, with a 95% confidence interval of (0.78, 0.85), is found around 5 GV, while at 1 GV, $r = 0.73$, with a 95% confidence interval of (0.68, 0.77). The correlation becomes consistent with zero at the 95% confidence level around 22 GV.

Panels (d) and (e) show the time variation of the low- and high-rigidity slope of the parallel diffusion coefficient, a_{\parallel} and b_{\parallel} . The best-fit values vary considerably from month to month, making it difficult to discern any clear time-dependent pattern. Indeed, sometimes the $\chi_{\min}^2(q)$ curve has two local minima or does not have a parabolic behavior. This means that these two parameters are not well constrained by fitting the AMS-02 proton fluxes, implying that the modulated flux is not so sensitive to the values of a_{\parallel} and b_{\parallel} for rigidities above 1 GV. A possible explanation is that the parallel diffusion dominates very close to the Sun, when most of the modulation has already happened. The diffusion coefficient in the radial direction is

$K_{rr} = k_{\parallel} \cos^2 \psi + k_{\perp,r} \sin^2 \psi$; imposing equality between the two terms yields $\tan^2 \psi \simeq 1/k_{\perp,r}^0 = 50$, corresponding to a spiral angle $\psi \approx 80^\circ$, which can already be found around 5 au, a mere 0.01% of the whole heliosphere volume. The time variation of GCR protons measured by PAMELA down to 400 MV (Adriani et al. 2013b; Martucci et al. 2018) would provide a better constraint on the slopes of the parallel diffusion coefficient; this study will be the focus of a future work.

The parameters describing the perpendicular diffusion coefficient, a_{\perp} and b_{\perp} , are shown in panels (f) and (g). Remarkably, b_{\perp} is almost constant with time for both positive and negative polarity, whose best-fit values agree in almost all of the overlapping months. Here a_{\perp} is mostly flat before the maximum of solar activity, when $A < 0$. During the period of the polarity reversal, a_{\perp} rises, almost doubling its value (with respect to 2011 and 2012) as the solar activity peaks, showing an anticorrelation with the proton flux at 1 GV (see the third panel). This suggests that, on top of the overall modulation scale determined by k_{\parallel}^0 , low rigidities experience an even smaller perpendicular mean free path. This is also supported by computing the Pearson correlation between a_{\perp} and the proton flux intensity at different rigidities: the maximum anticorrelation $r = -0.5$, with a 95% confidence interval of (-0.62, -0.39), is found at 1 GV, while it decreases with increasing rigidity, becoming consistent with zero above 20 GV. As for k_{\parallel}^0 , during the period of the polarity reversal, the best-fit a_{\perp} and b_{\perp} obtained from models with negative polarity agree, within the fit uncertainties, with the ones from models with positive polarity. We verified that these results do not depend on the duration of the period used to compute the backward average of the HMF and tilt angle (see Section 3.1). We varied the number of months (n) included in the average between zero and 24 months in steps of 2 months. For $n \geq 4$ months, the values of the best-fit parameters are consistent, within the uncertainties, with the ones presented in Figure 5, while the residuals between the best-fit models and the data are similar to the ones shown in Figure 4. For $n = 0$ and 2 months, the normalized χ^2 and the residuals are worse in a few BRs between the end of 2014 and the beginning of 2015, when the HMF has a higher variability than in the rest of the analyzed period. This suggests that the steady-state approximation is a valid approach to describe the time variation of GCRs above 1 GV on a monthly basis, provided the heliosphere status is adjusted by smoothing the input HMF and tilt angle with a backward average of at least 4 months.

5. p/He Ratio Comparison

It is generally assumed in modulation studies that the rigidity dependence of the three mean free paths is the same for all nuclei. The assumption has not been rigorously tested because the observational data were never accurate enough over the relevant rigidity range for all cosmic-ray nuclei over a complete solar cycle. Under this assumption, the best-fit parameters derived in Section 4 from AMS-02 protons should also be valid for other nuclei, in particular ^3He and ^4He . In order to compute the modeled p/He ratio, we ran the best-fit models for ^3He and ^4He (with the corresponding charge, mass, and LIS), and then we summed the resulting modulated fluxes.

Figure 6 shows the comparison between the p/He ratio observed by AMS-02 and the one predicted by the model. In the top left panel, three p/He AMS-02 ratios for the same BRs from Figure 4 are plotted as a function of rigidity (colored

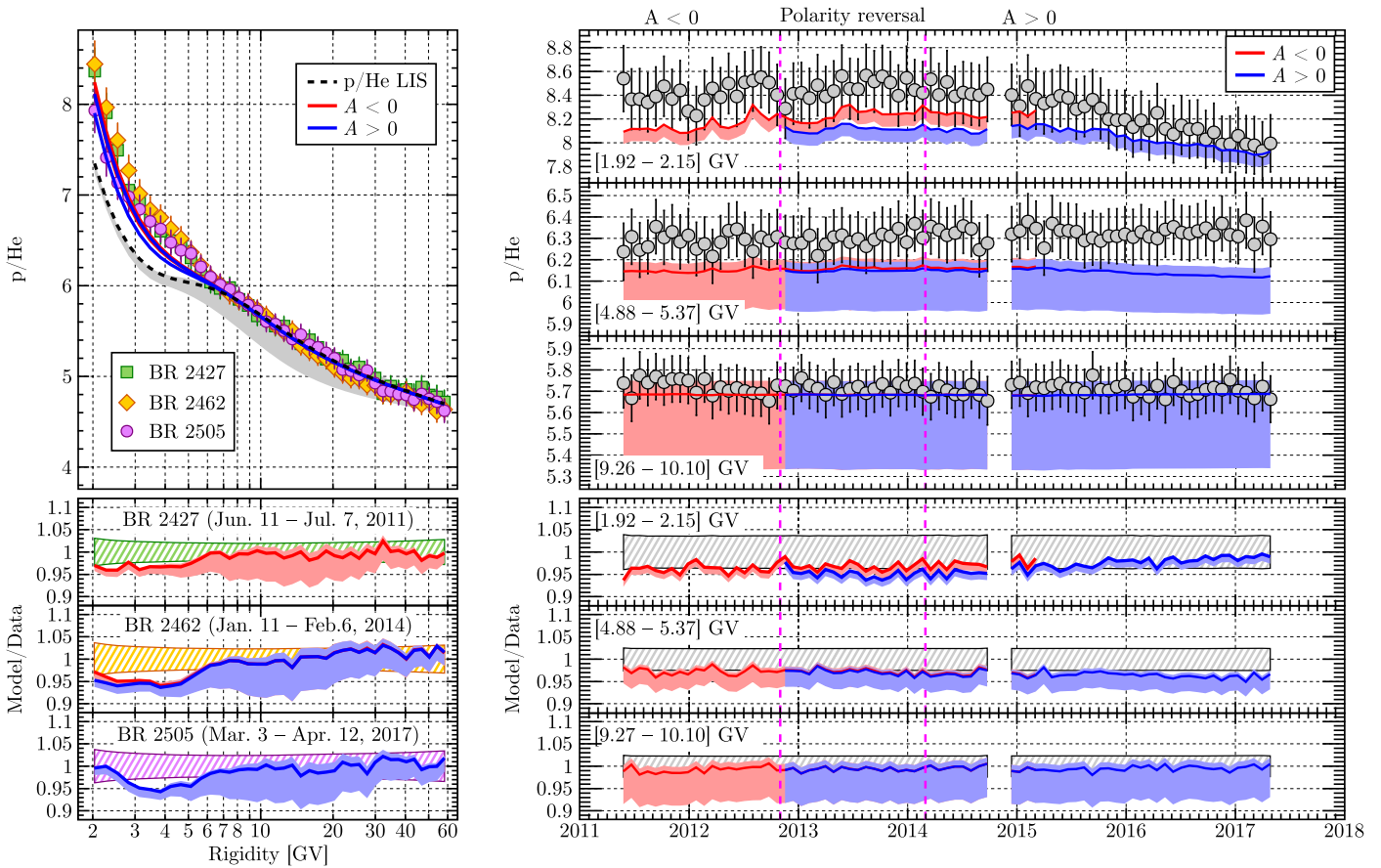


Figure 6. Top left: three selected AMS-02 p/He ratios (colored symbols) as a function of rigidity, together with their best-fit models (red and blue lines) and the p/He LIS (dashed black line). Bottom left: ratio of best-fit models to data for the three BRs (red and blue lines), compared to the corresponding AMS-02 uncertainties (green, orange, and magenta hatched regions). Light red, blue, and gray shaded regions represent the p/He uncertainty due to different ^3He and ^4He LIS parameterizations. Top right: three selected rigidity bins of the AMS-02 p/He ratio as a function of time (gray circles), together with their best-fit models (red and blue lines and bands). Bottom right: ratio of best-fit models to data for the three rigidity bins (red and blue lines and shaded regions), compared to the corresponding AMS-02 uncertainties (gray hatched regions). The vertical dashed magenta lines delimit the period of the solar magnetic field polarity reversal.

symbols), together with the best-fit models (blue and red lines, respectively, for negative and positive polarity models). For reference, the p/He LIS is also shown as a dashed black line. In the bottom left panel, the ratio between the best-fit models and data for the three selected BRs (red and blue lines) is shown and compared to the corresponding uncertainty on the AMS-02 p/He ratios (green, orange, and magenta hatched regions). The light red, blue, and gray shaded regions represent the uncertainty on p/He due to the uncertainty on the ^3He and ^4He LISs. This uncertainty has been estimated by varying the data sets used to derive the ^3He and ^4He LISs and assuming (or not) the same modulation potential for ^3He and ^4He (see Section 2.3). A total of 16 different LIS parameterizations have been computed, and for each of them, the best-fit models have been run. The minimum and maximum values among the different parameterizations at each rigidity have been considered as the uncertainty on the modulated p/He. While the difference in LIS parameterizations above 2 GV is between 10% and 60% for ^3He and between 5% and 10% for ^4He , the uncertainty on the modulated p/He is relatively small: less than 4%. For comparison, the uncertainty on the proton LIS coming from the parameterization fit is less than 2%, so its contribution to the modulated p/He uncertainty is considered negligible. In the following, the LIS parameterization described in Section 2.3 will be called the reference LIS.

In the top right panel of Figure 6, three rigidity bins of the AMS-02 p/He ratio as a function of time have been chosen (gray circles): [1.92–2.15], [4.88–5.37], and [9.26–10.10] GV. The best-fit models, together with their uncertainties, are shown as red (negative polarity models) and blue (positive polarity models) lines and shaded regions. In the bottom right panel, the ratio between the best-fit models and data for the three selected rigidity bins (red and blue lines and shaded regions) is shown, together with the corresponding uncertainty on the AMS-02 fluxes (gray hatched regions). We can see that the modeled p/He using the reference LIS on average underestimates the data by 5% below 6 GV. This difference remains basically constant in time, amounting to a rigidity-dependent normalization shift in the modulated p/He below 6 GV, which persists even considering the modeled p/He uncertainties. Indeed, the different LIS parameterizations result in similar p/He time variations, differing only for a shift constant in time. This might be due to two reasons: (a) the ^3He and ^4He LIS parameterizations are not correct below 5 GV, and (b) the assumption of same mean free path for p and He at all relevant rigidities is inadequate. We believe that (a) is the most probable explanation; indeed, the use of the force-field approximation to derive the LIS might introduce a bias in the resulting parameterization, which could affect the results of the numerical model analysis.

6. Time Dependence of p/He

The AMS-02 data show that above 3 GV, the p/He ratio is time-independent. Below 3 GV, it is flat within month-to-month variations until 2015 March, and then it starts to decrease, seemingly correlated with the decrease in solar activity. As stated in Aguilar et al. (2018), the origin of the p/He time dependence may be due to (a) the difference in LIS shape between p and He and (b) the dependence of the diffusion tensor on the particle mass-to-charge ratio, A/Z . For the sake of simplicity, let us examine the steady-state one-dimensional version of the Parker equation,

$$V \frac{\partial f}{\partial r} - \frac{1}{r^2} \frac{\partial}{\partial r} \left(kr^2 \frac{\partial f}{\partial r} \right) - \frac{R}{3r^2} \frac{\partial}{\partial r} (r^2 V) \frac{\partial f}{\partial R} = 0, \quad (15)$$

where V is the solar wind speed and $k = k(r, R, A/Z) = \frac{1}{3} v(R, A/Z) \lambda(r, R)$ is the radial diffusion coefficient. Here $v(R, A/Z) = \beta c = c / \sqrt{1 + (A/Z)^2 (mc/eR)^2}$ is the particle velocity, with m the proton rest mass, while $\lambda(r, R)$ is the mean free path, which is assumed to depend only on the radial distance and rigidity, i.e., to be the same for all nuclei.

Let us assume that two nuclei, p_1 and p_2 , have the same A/Z but a different LIS shape: then the diffusion coefficient will be the same for both, but the boundary conditions will not be equal. In particular, the last term is sensitive to the spectral index, $\Gamma = \partial \log(f) / \partial \log(R) = R/f \partial f / \partial R$, so we can expect that the difference in Γ at the heliopause will persist during the propagation through the heliosphere. Since V and k change with varying modulation conditions, $\Gamma(p_1/p_2) = \Gamma(p_1) - \Gamma(p_2)$ will be changing as well; i.e., the ratio p_1/p_2 at a given rigidity will not be constant in time. Now let us assume that two nuclei with different A/Z have the same LIS shape; then all the terms in the Parker equation are the same for the two species, except for the divergence of the diffusive flux, because of the A/Z dependence of k . A time variation of k will translate into a time variation of p_1/p_2 at a given rigidity. It is important to note that this dependence comes from the fact that we assumed λ to depend only on R ; if λ was also a function of A and Z , the A/Z dependence of $v\lambda$ might cancel out. Effectively, we can say that if two nuclei with different A/Z have the same mean free path, then the time variation of p_1/p_2 is a natural consequence, even when the LIS shape is the same.

The same reasoning can be applied to the full 3D case. The symmetric components of the field-aligned diffusion tensor K can all be written as $k_i = \frac{1}{3} v \lambda_i$, where i stands for the parallel, perpendicular radial, and perpendicular polar directions, so that K also depends explicitly on A/Z .

In the case of p/He, all of the species involved have different A/Z and LISs, so the time dependence is due to a combination of (a) and (b). To assess which of the two causes is dominant, we separately test the effect of (a) and (b). Since the uncertainties on the ${}^3\text{He}$ and ${}^4\text{He}$ LIS parameterizations do not affect the modeled p/He time dependence at a given rigidity, but only its normalization, in the rest of this section, we will use the reference LIS and compare the normalized modeled p/He to the normalized observed p/He, in order to remove any normalization shift. We verified that the uncertainty on the normalized p/He due to the uncertainty in the ${}^3\text{He}$ and ${}^4\text{He}$ LISs is less than 0.5% at all rigidities and for each BR.

6.1. Difference in the LIS Shape

To understand the effect of the difference in the LIS shape, we ran the best-fit models for p, ${}^3\text{He}$, and ${}^4\text{He}$, forcing the same A/Z for all three species but using the appropriate LIS for each particle. In the following, p corresponds to the proton LIS and $A/Z = 1$, ${}^3\text{He}$ corresponds to the ${}^3\text{He}$ LIS and $A/Z = 1$, while ${}^4\text{He}$ corresponds to the ${}^4\text{He}$ LIS and $A/Z = 1$. The same results are obtained if we use $A/Z = 3/2$ or 2 for all particles.

Figure 7 shows the comparison of the normalized modeled $p/{}^3\text{He}$ (red and blue lines; left panels) and $p/{}^4\text{He}$ (red and blue lines; right panels) with the normalized observed p/He (gray circles) for three selected rigidity bins: [1.92–2.15], [2.40–2.67], and [2.97–3.29] GV. Note that the plotted experimental uncertainties are the sum in quadrature of the statistical and time-dependent uncertainties only; the systematic uncertainties constant in time are not considered here, since they would affect only the average value of p/He in a given rigidity bin, not its time variation.

The time trend of the observed p/He is not reproduced: $p/{}^4\text{He}$ increases with time at all rigidities after 2015 March, while $p/{}^3\text{He}$ increases at 2 GV, stays flat at 2.5 GV, and slightly decreases at 3 GV.

We can better understand the different behavior of $p/{}^3\text{He}$ and $p/{}^4\text{He}$ by looking at the spectral index, Γ , of the LIS ratio. Because of the adiabatic energy losses, the observed particles at 2 GV had a greater rigidity before entering the heliosphere, so in order to compare Γ in interstellar space, we should correct for this effect. In the force-field approximation framework, the energy losses are related to the modulation potential ϕ , whose values usually vary between a few hundred MV and 1 GV, depending on the level of solar activity. Using $\phi = 400$ MV as the average modulation potential in the descending phase of the solar cycle, we can relate the rigidity observed at Earth $R_E = \sqrt{T_E(T_E + 2Amc^2)}/Ze$ with the rigidity at the heliopause $R_{HP} = \sqrt{T_{HP}(T_{HP} + 2Amc^2)}/Ze$, where $T_{HP} = T_E + Ze\phi$, while T_E and T_{HP} are, respectively, the kinetic energy at Earth and the heliopause. With this choice, we find that at 2 GV, $\Gamma(p/{}^3\text{He}) = -0.25$, while $\Gamma(p/{}^4\text{He}) = -0.39$; at 2.5 GV, $\Gamma(p/{}^3\text{He}) = -0.03$, while $\Gamma(p/{}^4\text{He}) = -0.26$; and at 3 GV, $\Gamma(p/{}^3\text{He}) = 0.12$, while $\Gamma(p/{}^4\text{He}) = -0.16$. Note that when the values of $\Gamma(p/{}^3\text{He})$ and $\Gamma(p/{}^4\text{He})$ are very similar in absolute value, so is the amplitude of the time variation in the normalized modeled ratios. A different choice of ϕ leads to different values for Γ , but qualitatively, the comparison remains the same: $\Gamma(p/{}^4\text{He})$ is always negative and decreases in absolute value with increasing rigidity, while $\Gamma(p/{}^3\text{He})$ is negative at 2 GV, very close to zero at 2.5 GV, and positive at 3 GV. This suggests that the time behavior of the ratio of two species with the same A/Z is related to the spectral index of the LIS ratio of the two species: if $\Gamma < 0$, then the ratio will be anticorrelated with the solar activity, while if $\Gamma > 0$, the ratio will be correlated with the solar activity. The amplitude of the time variation is instead proportional to the absolute value of Γ . We verified that this result holds when considering different parameterizations for the ${}^3\text{He}$ and ${}^4\text{He}$ LISs. The uncertainties on the ${}^4\text{He}$ LIS are small enough that $\Gamma(p/{}^4\text{He})$ is always negative, leading to an increase of $p/{}^4\text{He}$. Instead, the uncertainties on the ${}^3\text{He}$ LIS are such that $\Gamma(p/{}^3\text{He})$ can be positive or negative depending on the parameterization, so $p/{}^3\text{He}$ decreases or increases with time according to the sign of $\Gamma(p/{}^3\text{He})$. Since ${}^4\text{He}$ accounts for around 80% of the He, the

Table 2
Best-fit Parameters Used as Input for Numerical Models with Negative Polarity

BR ^a	α^b	B_0^c	k_{\parallel}^{0d}	$\lambda_{\perp}(1 \text{ GV})^e$	$\lambda_{\perp}(5 \text{ GV})^e$	a_{\parallel}^f	b_{\parallel}^g	a_{\perp}^h	b_{\perp}^i
2426	51.20	4.85	110_{-5}^{+20}	$0.009_{-0.003}^{+0.003}$	$0.034_{-0.004}^{+0.005}$	$0.8_{-0.2}^{+0.2}$	$1.7_{-0.2}^{+0.2}$	$0.8_{-0.2}^{+0.2}$	$0.8_{-0.2}^{+0.1}$
2427	53.55	4.87	110_{-5}^{+4}	$0.006_{-0.002}^{+0.005}$	$0.032_{-0.003}^{+0.002}$	≤ 0.3	$1.7_{-0.1}^{+0.1}$	$1.1_{-0.05}^{+0.05}$	$0.8_{-0.06}^{+0.08}$
2428	55.33	4.93	110_{-4}^{+9}	$0.009_{-0.002}^{+0.003}$	$0.034_{-0.002}^{+0.004}$	$1.1_{-0.1}^{+0.1}$	$2_{-0.2}^{+0.2}$	$0.8_{-0.1}^{+0.2}$	$0.8_{-0.1}^{+0.1}$
2429	57.05	4.96	110_{-5}^{+20}	$0.009_{-0.002}^{+0.003}$	$0.033_{-0.003}^{+0.005}$	$1.1_{-0.2}^{+0.2}$	$2_{-0.3}^{+0.3}$	$0.8_{-0.1}^{+0.2}$	$0.8_{-0.1}^{+0.1}$
2430	58.67	5.05	130_{-10}^{+6}	$0.011_{-0.002}^{+0.005}$	$0.039_{-0.004}^{+0.004}$	≥ 1.8	$1.4_{-0.07}^{+0.2}$	$0.8_{-0.1}^{+0.3}$	$0.8_{-0.09}^{+0.1}$
2431	60.34	5.10	110_{-4}^{+5}	$0.009_{-0.008}^{+0.003}$	$0.032_{-0.002}^{+0.003}$	$1.4_{-0.1}^{+0.1}$	$2_{-0.2}^{+0.1}$	$0.8_{-0.05}^{+0.2}$	$0.8_{-0.08}^{+0.06}$
2432	62.13	5.13	130_{-7}^{+4}	$0.011_{-0.001}^{+0.004}$	$0.038_{-0.002}^{+0.003}$	≥ 1.9	$1.4_{-0.04}^{+0.1}$	$0.8_{-0.08}^{+0.3}$	$0.8_{-0.07}^{+0.07}$
2433	63.64	5.14	130_{-5}^{+10}	$0.007_{-0.003}^{+0.002}$	$0.035_{-0.003}^{+0.003}$	$0.5_{-0.2}^{+0.1}$	$1.7_{-0.1}^{+0.2}$	$1.1_{-0.2}^{+0.2}$	$0.8_{-0.08}^{+0.08}$
2434	64.97	5.19	130_{-6}^{+10}	$0.007_{-0.002}^{+0.002}$	$0.035_{-0.003}^{+0.004}$	$0.5_{-0.2}^{+0.1}$	$2_{-0.3}^{+0.1}$	$1.1_{-0.2}^{+0.2}$	$0.8_{-0.09}^{+0.1}$
2435	66.09	5.24	130_{-8}^{+6}	$0.01_{-0.002}^{+0.004}$	$0.037_{-0.003}^{+0.003}$	$1.7_{-0.2}^{+0.2}$	$1.4_{-0.07}^{+0.3}$	$0.8_{-0.1}^{+0.3}$	$0.8_{-0.09}^{+0.1}$
2436	66.48	5.34	130_{-10}^{+7}	$0.01_{-0.002}^{+0.004}$	$0.037_{-0.004}^{+0.004}$	$1.7_{-0.1}^{+0.2}$	$1.4_{-0.09}^{+0.3}$	$0.8_{-0.1}^{+0.3}$	$0.8_{-0.1}^{+0.2}$
2437	66.29	5.40	110_{-20}^{+6}	$0.008_{-0.003}^{+0.004}$	$0.031_{-0.005}^{+0.004}$	$1.7_{-0.1}^{+0.3}$	$1.7_{-0.1}^{+0.2}$	$0.8_{-0.2}^{+0.3}$	$0.8_{-0.09}^{+0.2}$
2438	66.25	5.35	130_{-9}^{+6}	$0.006_{-0.003}^{+0.001}$	$0.034_{-0.003}^{+0.003}$	$1.1_{-0.2}^{+0.1}$	$1.7_{-0.1}^{+0.2}$	$1.1_{-0.1}^{+0.2}$	$0.8_{-0.08}^{+0.1}$
2439	66.79	5.38	130_{-5}^{+10}	$0.006_{-0.002}^{+0.002}$	$0.034_{-0.003}^{+0.003}$	$0.8_{-0.2}^{+0.09}$	$1.7_{-0.1}^{+0.3}$	$1.1_{-0.2}^{+0.2}$	$0.8_{-0.09}^{+0.09}$
2440	67.54	5.45	130_{-20}^{+7}	$0.006_{-0.003}^{+0.002}$	$0.033_{-0.003}^{+0.004}$	$1.1_{-0.2}^{+0.2}$	$1.4_{-0.09}^{+0.3}$	$1.1_{-0.1}^{+0.2}$	$0.8_{-0.1}^{+0.2}$
2441	68.22	5.47	110_{-4}^{+10}	$0.005_{-0.002}^{+0.003}$	$0.028_{-0.002}^{+0.003}$	≤ 0.34	$2_{-0.1}^{+0.2}$	$1.1_{-0.2}^{+0.2}$	$0.8_{-0.07}^{+0.1}$
2442	68.70	5.48	90_{-5}^{+20}	$0.007_{-0.001}^{+0.003}$	$0.028_{-0.004}^{+0.006}$	$1.1_{-0.2}^{+0.2}$	$1.7_{-0.2}^{+0.2}$	$0.8_{-0.1}^{+0.3}$	$1.1_{-0.3}^{+0.07}$
2443	69.02	5.53	110_{-9}^{+8}	$0.008_{-0.002}^{+0.004}$	$0.03_{-0.003}^{+0.004}$	≥ 1.9	$2_{-0.1}^{+0.3}$	$0.8_{-0.1}^{+0.3}$	$0.8_{-0.06}^{+0.1}$
2444	69.31	5.57	130_{-20}^{+6}	$0.006_{-0.002}^{+0.002}$	$0.033_{-0.005}^{+0.005}$	$1.7_{-0.2}^{+0.2}$	$1.7_{-0.3}^{+0.2}$	$1.1_{-0.3}^{+0.2}$	$0.8_{-0.09}^{+0.3}$
2445	69.39	5.54	110_{-7}^{+10}	$0.008_{-0.001}^{+0.004}$	$0.03_{-0.002}^{+0.005}$	≥ 1.9	≥ 2.1	$0.8_{-0.08}^{+0.3}$	$0.8_{-0.07}^{+0.2}$
2446	68.95	5.52	110_{-8}^{+20}	$0.005_{-0.002}^{+0.002}$	$0.028_{-0.003}^{+0.006}$	$0.8_{-0.1}^{+0.3}$	≥ 2.1	$1.1_{-0.3}^{+0.3}$	$0.8_{-0.09}^{+0.4}$
2447	69.39	5.48	130_{-10}^{+6}	$0.0041_{-0.002}^{+0.003}$	$0.031_{-0.004}^{+0.003}$	$0.8_{-0.1}^{+0.1}$	$1.7_{-0.2}^{+0.2}$	$1.4_{-0.3}^{+0.08}$	$0.8_{-0.08}^{+0.2}$
2448	69.57	5.51	130_{-5}^{+7}	$0.004_{-0.002}^{+0.006}$	$0.031_{-0.002}^{+0.002}$	$0.50_{-0.1}^{+0.07}$	$2_{-0.2}^{+0.1}$	$1.4_{-0.2}^{+0.1}$	$0.8_{-0.06}^{+0.09}$
2449	69.31	5.49	130_{-5}^{+10}	$0.0063_{-0.0006}^{+0.003}$	$0.033_{-0.002}^{+0.004}$	$1.4_{-0.1}^{+0.08}$	$2_{-0.1}^{+0.1}$	$1.1_{-0.06}^{+0.3}$	$0.8_{-0.07}^{+0.1}$
2450	69.96	5.48	130_{-6}^{+4}	$0.0063_{-0.0007}^{+0.002}$	$0.033_{-0.002}^{+0.002}$	$1.4_{-0.09}^{+0.07}$	$1.7_{-0.1}^{+0.1}$	$1.1_{-0.06}^{+0.2}$	$0.8_{-0.05}^{+0.08}$
2451	70.68	5.38	110_{-20}^{+30}	$0.005_{-0.002}^{+0.002}$	$0.029_{-0.002}^{+0.005}$	$0.8_{-0.2}^{+0.2}$	≥ 2	$1.1_{-0.3}^{+0.3}$	$0.8_{-0.09}^{+0.1}$
2452	71.08	5.36	110_{-5}^{+10}	$0.005_{-0.002}^{+0.002}$	$0.029_{-0.002}^{+0.004}$	$0.8_{-0.1}^{+0.2}$	$2_{-0.1}^{+0.2}$	$1.1_{-0.2}^{+0.2}$	$0.8_{-0.08}^{+0.1}$
2453	71.09	5.38	90_{-5}^{+9}	$0.0045_{-0.002}^{+0.009}$	$0.023_{-0.002}^{+0.003}$	$0.5_{-0.1}^{+0.2}$	≥ 2.2	$1.1_{-0.1}^{+0.2}$	$0.8_{-0.07}^{+0.2}$
2454	70.97	5.36	90_{-5}^{+20}	$0.004_{-0.001}^{+0.002}$	$0.026_{-0.004}^{+0.006}$	$0.8_{-0.2}^{+0.2}$	$1.7_{-0.08}^{+0.3}$	$1.1_{-0.3}^{+0.2}$	$1.1_{-0.3}^{+0.07}$
2455	70.59	5.40	110_{-8}^{+5}	$0.005_{-0.001}^{+0.002}$	$0.028_{-0.003}^{+0.002}$	$1.7_{-0.1}^{+0.2}$	$2_{-0.2}^{+0.1}$	$1.1_{-0.1}^{+0.3}$	$0.8_{-0.06}^{+0.1}$
2456	70.25	5.31	110_{-10}^{+6}	$0.006_{-0.001}^{+0.002}$	$0.029_{-0.004}^{+0.004}$	≥ 1.8	$2_{-0.2}^{+0.2}$	$1.1_{-0.2}^{+0.2}$	$0.8_{-0.08}^{+0.2}$
2457	70.09	5.26	90_{-4}^{+20}	$0.003_{-0.001}^{+0.001}$	$0.025_{-0.003}^{+0.005}$	≤ 0.35	$2_{-0.2}^{+0.2}$	$1.4_{-0.3}^{+0.2}$	$1.1_{-0.3}^{+0.09}$
2458	69.75	5.20	110_{-10}^{+9}	$0.004_{-0.001}^{+0.001}$	$0.027_{-0.003}^{+0.004}$	$1.1_{-0.1}^{+0.2}$	≥ 2.1	$1.4_{-0.3}^{+0.3}$	$0.8_{-0.07}^{+0.2}$
2459	69.38	5.16	110_{-10}^{+9}	$0.004_{-0.001}^{+0.002}$	$0.028_{-0.003}^{+0.003}$	$1.1_{-0.1}^{+0.2}$	$2_{-0.1}^{+0.3}$	$1.4_{-0.2}^{+0.3}$	$0.8_{-0.07}^{+0.2}$
2460	69.35	5.18	110_{-10}^{+6}	$0.0023_{-0.001}^{+0.003}$	$0.026_{-0.003}^{+0.002}$	≤ 0.37	$2_{-0.2}^{+0.2}$	$1.7_{-0.3}^{+0.09}$	$0.8_{-0.07}^{+0.2}$
2461	69.19	5.17	110_{-8}^{+6}	$0.0036_{-0.0007}^{+0.003}$	$0.028_{-0.002}^{+0.003}$	$1.4_{-0.2}^{+0.1}$	$2_{-0.2}^{+0.1}$	$1.4_{-0.1}^{+0.2}$	$0.8_{-0.08}^{+0.1}$
2462	68.89	5.22	110_{-4}^{+5}	$0.0023_{-0.001}^{+0.003}$	$0.025_{-0.002}^{+0.001}$	≤ 0.28	$2_{-0.1}^{+0.1}$	$1.7_{-0.3}^{+0.07}$	$0.8_{-0.06}^{+0.06}$
2463	68.43	5.33	90_{-5}^{+10}	$0.0029_{-0.001}^{+0.001}$	$0.022_{-0.002}^{+0.004}$	≤ 0.41	≥ 2.1	$1.4_{-0.3}^{+0.2}$	$0.8_{-0.1}^{+0.2}$
2464	68.01	5.29	110_{-10}^{+5}	$0.0036_{-0.001}^{+0.001}$	$0.027_{-0.004}^{+0.003}$	$1.4_{-0.2}^{+0.1}$	$2_{-0.2}^{+0.2}$	$1.4_{-0.2}^{+0.2}$	$0.8_{-0.08}^{+0.2}$
2465	67.03	5.34	110_{-10}^{+6}	$0.004_{-0.001}^{+0.002}$	$0.027_{-0.004}^{+0.003}$	$1.1_{-0.1}^{+0.2}$	$1.7_{-0.08}^{+0.3}$	$1.4_{-0.1}^{+0.3}$	$0.8_{-0.1}^{+0.2}$
2466	65.73	5.35	110_{-5}^{+10}	$0.0035_{-0.001}^{+0.009}$	$0.027_{-0.002}^{+0.003}$	$0.8_{-0.1}^{+0.1}$	≥ 2.1	$1.4_{-0.3}^{+0.2}$	$0.8_{-0.07}^{+0.1}$
2467	64.25	5.34	110_{-4}^{+3}	$0.0055_{-0.0004}^{+0.002}$	$0.029_{-0.001}^{+0.002}$	≥ 1.9	$2_{-0.2}^{+0.1}$	$1.1_{-0.04}^{+0.2}$	$0.8_{-0.05}^{+0.06}$
2468	63.14	5.30	110_{-10}^{+6}	$0.004_{-0.001}^{+0.001}$	$0.027_{-0.004}^{+0.003}$	$1.1_{-0.1}^{+0.2}$	$1.7_{-0.09}^{+0.2}$	$1.4_{-0.2}^{+0.2}$	$0.8_{-0.09}^{+0.2}$
2469	62.32	5.20	110_{-5}^{+9}	$0.0036_{-0.001}^{+0.008}$	$0.027_{-0.003}^{+0.003}$	$0.8_{-0.1}^{+0.1}$	$2_{-0.2}^{+0.1}$	$1.4_{-0.1}^{+0.3}$	$0.8_{-0.1}^{+0.09}$
2470	62.20	5.29	110_{-6}^{+20}	$0.004_{-0.001}^{+0.001}$	$0.027_{-0.003}^{+0.005}$	≤ 0.41	$2_{-0.3}^{+0.2}$	$1.4_{-0.3}^{+0.3}$	$0.8_{-0.1}^{+0.1}$
2471	62.36	5.40	110_{-6}^{+20}	$0.003_{-0.001}^{+0.001}$	$0.026_{-0.004}^{+0.005}$	≤ 0.38	$2_{-0.3}^{+0.2}$	$1.4_{-0.3}^{+0.2}$	$0.8_{-0.09}^{+0.1}$
2474	59.85	5.87	110_{-3}^{+9}	$0.0078_{-0.0006}^{+0.003}$	$0.028_{-0.002}^{+0.003}$	$1.7_{-0.2}^{+0.2}$	$1.7_{-0.1}^{+0.2}$	$0.8_{-0.05}^{+0.2}$	$0.8_{-0.1}^{+0.05}$
2475	58.91	6.04	110_{-5}^{+20}	$0.0076_{-0.001}^{+0.004}$	$0.027_{-0.002}^{+0.005}$	$1.7_{-0.2}^{+0.2}$	$2_{-0.2}^{+0.3}$	$0.8_{-0.08}^{+0.3}$	$0.8_{-0.2}^{+0.2}$
2476	57.80	6.17	130_{-20}^{+7}	$0.006_{-0.002}^{+0.002}$	$0.029_{-0.004}^{+0.004}$	$1.4_{-0.1}^{+0.2}$	$1.4_{-0.1}^{+0.2}$	$1.1_{-0.2}^{+0.2}$	$0.8_{-0.1}^{+0.2}$
2477	56.43	6.18	110_{-4}^{+7}	$0.0047_{-0.002}^{+0.008}$	$0.022_{-0.002}^{+0.002}$	$0.8_{-0.1}^{+0.1}$	$2_{-0.1}^{+0.2}$	$1.1_{-0.2}^{+0.1}$	$0.8_{-0.07}^{+0.2}$

Notes. A \leq (\geq) symbol means that the best-fit value for the parameter coincides with the lower (upper) edge of the grid, so a lower (upper) limit is reported, corresponding to $\hat{q}_n + q_{n,r}$

($\hat{q}_n - q_{n,l}$).

^a BR number.

^b Tilt angle, in units of degrees.

^c HMF intensity at Earth, in units of nT.

^d Normalization of the parallel diffusion coefficient, in units of $6 \times 10^{20} \text{ cm}^2 \text{ s}^{-1}$.

^e Perpendicular mean free path at 1 and 5 GV at Earth, in units of au. The uncertainty is computed by propagating the uncertainties on k_{\parallel}^0 , a_{\perp} , and b_{\perp} .

^f Low-rigidity slope of the parallel diffusion coefficient.

^g High-rigidity slope of the parallel diffusion coefficient.

^h Low-rigidity slope of the perpendicular diffusion coefficient.

ⁱ High-rigidity slope of the perpendicular diffusion coefficient.

Table 3
Best-fit Parameters Used as Input for Numerical Models with Positive Polarity

BR	α	B_0	k_{\parallel}^0	λ_{\perp} (1 GV)	λ_{\perp} (5 GV)	a_{\parallel}	b_{\parallel}	a_{\perp}	b_{\perp}
2446	68.95	5.52	110^{+10}_{-9}	$0.005^{+0.001}_{-0.001}$	$0.028^{+0.004}_{-0.003}$	$1.7^{+0.3}_{-0.3}$	≥ 2.1	$1.1^{+0.2}_{-0.1}$	$0.8^{+0.1}_{-0.06}$
2447	69.39	5.48	130^{+5}_{-10}	$0.0041^{+0.0005}_{-0.001}$	$0.031^{+0.002}_{-0.003}$	$1.1^{+0.3}_{-0.2}$	$1.4^{+0.3}_{-0.2}$	$1.4^{+0.08}_{-0.08}$	$0.8^{+0.1}_{-0.08}$
2448	69.57	5.51	130^{+6}_{-6}	$0.004^{+0.0006}_{-0.0006}$	$0.031^{+0.002}_{-0.002}$	$0.5^{+0.2}_{-0.1}$	$2^{+0.2}_{-0.2}$	$1.4^{+0.1}_{-0.1}$	$0.8^{+0.09}_{-0.04}$
2449	69.31	5.49	130^{+7}_{-7}	$0.0041^{+0.0005}_{-0.001}$	$0.031^{+0.002}_{-0.003}$	≤ 0.38	$2^{+0.3}_{-0.2}$	$1.4^{+0.08}_{-0.2}$	$0.8^{+0.1}_{-0.05}$
2450	69.96	5.48	130^{+6}_{-6}	$0.0041^{+0.0005}_{-0.001}$	$0.031^{+0.002}_{-0.003}$	≤ 0.44	$1.4^{+0.3}_{-0.3}$	$1.4^{+0.2}_{-0.2}$	$0.8^{+0.07}_{-0.09}$
2451	70.68	5.38	110^{+5}_{-5}	$0.0055^{+0.0007}_{-0.0006}$	$0.029^{+0.002}_{-0.001}$	$1.4^{+0.3}_{-0.2}$	≥ 2	$1.1^{+0.08}_{-0.07}$	$0.8^{+0.07}_{-0.04}$
2452	71.08	5.36	110^{+5}_{-6}	$0.0055^{+0.001}_{-0.0008}$	$0.029^{+0.002}_{-0.002}$	$1.7^{+0.3}_{-0.3}$	≥ 2	$1.1^{+0.1}_{-0.09}$	$0.8^{+0.09}_{-0.05}$
2453	71.09	5.38	90^{+7}_{-20}	$0.004^{+0.001}_{-0.002}$	$0.023^{+0.003}_{-0.005}$	$1.7^{+0.3}_{-0.3}$	≥ 2	$1.1^{+0.2}_{-0.3}$	$0.8^{+0.3}_{-0.08}$
2454	70.97	5.36	90^{+20}_{-10}	$0.004^{+0.002}_{-0.002}$	$0.023^{+0.006}_{-0.004}$	$1.7^{+0.3}_{-0.3}$	≥ 2.1	$1.1^{+0.3}_{-0.2}$	$0.8^{+0.2}_{-0.1}$
2455	70.59	5.40	110^{+5}_{-3}	$0.0035^{+0.0007}_{-0.0007}$	$0.026^{+0.002}_{-0.002}$	≥ 1.7	$1.7^{+0.3}_{-0.1}$	$1.4^{+0.1}_{-0.1}$	$0.8^{+0.1}_{-0.07}$
2456	70.25	5.31	110^{+9}_{-20}	$0.004^{+0.001}_{-0.001}$	$0.027^{+0.004}_{-0.005}$	≥ 1.7	$1.7^{+0.3}_{-0.2}$	$1.4^{+0.3}_{-0.2}$	$0.8^{+0.3}_{-0.1}$
2457	70.09	5.26	90^{+10}_{-5}	$0.0029^{+0.0009}_{-0.0004}$	$0.025^{+0.004}_{-0.002}$	$0.5^{+0.3}_{-0.2}$	$1.4^{+0.2}_{-0.2}$	$1.4^{+0.2}_{-0.08}$	$1.1^{+0.2}_{-0.2}$
2458	69.75	5.20	110^{+10}_{-20}	$0.0023^{+0.0005}_{-0.0009}$	$0.026^{+0.003}_{-0.004}$	≤ 0.44	≥ 2.1	$1.7^{+0.1}_{-0.2}$	$0.8^{+0.2}_{-0.07}$
2459	69.38	5.16	110^{+8}_{-10}	$0.0023^{+0.0004}_{-0.0007}$	$0.026^{+0.003}_{-0.003}$	≤ 0.46	≥ 2.1	$1.7^{+0.1}_{-0.2}$	$0.8^{+0.2}_{-0.06}$
2460	69.35	5.18	110^{+7}_{-10}	$0.0023^{+0.0004}_{-0.0006}$	$0.026^{+0.002}_{-0.003}$	$0.5^{+0.3}_{-0.2}$	≥ 2	$1.7^{+0.1}_{-0.2}$	$0.8^{+0.2}_{-0.05}$
2461	69.19	5.17	110^{+5}_{-6}	$0.0023^{+0.0003}_{-0.0004}$	$0.026^{+0.002}_{-0.002}$	$0.8^{+0.3}_{-0.3}$	$2^{+0.3}_{-0.3}$	$1.7^{+0.08}_{-0.1}$	$0.8^{+0.1}_{-0.05}$
2462	68.89	5.22	110^{+6}_{-5}	$0.0023^{+0.0003}_{-0.0003}$	$0.025^{+0.002}_{-0.001}$	≤ 0.47	$2^{+0.2}_{-0.3}$	$1.7^{+0.09}_{-0.07}$	$0.8^{+0.07}_{-0.05}$
2463	68.43	5.33	90^{+10}_{-10}	$0.0029^{+0.001}_{-0.0007}$	$0.022^{+0.004}_{-0.003}$	$0.8^{+0.3}_{-0.3}$	≥ 2.1	$1.4^{+0.2}_{-0.1}$	$0.8^{+0.1}_{-0.09}$
2464	68.01	5.29	110^{+7}_{-10}	$0.0023^{+0.0004}_{-0.0006}$	$0.025^{+0.002}_{-0.003}$	$1.7^{+0.3}_{-0.3}$	$2^{+0.3}_{-0.3}$	$1.7^{+0.1}_{-0.2}$	$0.8^{+0.2}_{-0.06}$
2465	67.03	5.34	110^{+6}_{-9}	$0.0023^{+0.0004}_{-0.0005}$	$0.025^{+0.002}_{-0.002}$	$0.5^{+0.2}_{-0.3}$	$2^{+0.2}_{-0.3}$	$1.7^{+0.1}_{-0.1}$	$0.8^{+0.1}_{-0.05}$
2466	65.73	5.35	130^{+6}_{-10}	$0.0027^{+0.0004}_{-0.0007}$	$0.029^{+0.002}_{-0.003}$	$1.7^{+0.3}_{-0.3}$	$1.4^{+0.2}_{-0.2}$	$1.7^{+0.1}_{-0.2}$	$0.8^{+0.1}_{-0.09}$
2467	64.25	5.34	110^{+10}_{-10}	$0.0023^{+0.0006}_{-0.0006}$	$0.025^{+0.003}_{-0.003}$	≤ 0.4	≥ 2	$1.7^{+0.2}_{-0.2}$	$0.8^{+0.2}_{-0.2}$
2468	63.14	5.30	110^{+6}_{-20}	$0.0023^{+0.0003}_{-0.0005}$	$0.025^{+0.002}_{-0.002}$	≤ 0.48	$2^{+0.3}_{-0.3}$	$1.7^{+0.09}_{-0.1}$	$0.8^{+0.1}_{-0.05}$
2469	62.32	5.20	130^{+20}_{-20}	$0.003^{+0.001}_{-0.001}$	$0.03^{+0.005}_{-0.005}$	$1.7^{+0.3}_{-0.3}$	$1.4^{+0.3}_{-0.2}$	$1.7^{+0.2}_{-0.2}$	$0.8^{+0.2}_{-0.2}$
2470	62.20	5.29	130^{+8}_{-10}	$0.0027^{+0.0003}_{-0.0008}$	$0.03^{+0.002}_{-0.003}$	≤ 0.39	$1.1^{+0.2}_{-0.04}$	$1.7^{+0.06}_{-0.1}$	$0.8^{+0.07}_{-0.1}$
2471	62.36	5.40	110^{+20}_{-7}	$0.0035^{+0.002}_{-0.0006}$	$0.026^{+0.005}_{-0.003}$	≤ 0.49	$2^{+0.3}_{-0.3}$	$1.4^{+0.3}_{-0.1}$	$0.8^{+0.1}_{-0.2}$
2474	59.85	5.87	110^{+5}_{-5}	$0.005^{+0.0005}_{-0.0003}$	$0.026^{+0.001}_{-0.001}$	$1.7^{+0.3}_{-0.3}$	$1.7^{+0.2}_{-0.3}$	$1.1^{+0.07}_{-0.04}$	$0.8^{+0.04}_{-0.07}$
2475	58.91	6.04	110^{+20}_{-5}	$0.0049^{+0.002}_{-0.0006}$	$0.025^{+0.005}_{-0.002}$	$1.4^{+0.3}_{-0.3}$	≥ 2	$1.1^{+0.3}_{-0.08}$	$0.8^{+0.08}_{-0.1}$
2476	57.80	6.17	130^{+4}_{-9}	$0.0036^{+0.0003}_{-0.0008}$	$0.027^{+0.001}_{-0.002}$	$0.5^{+0.3}_{-0.2}$	$1.1^{+0.2}_{-0.05}$	$1.4^{+0.06}_{-0.1}$	$0.8^{+0.07}_{-0.06}$
2477	56.43	6.18	110^{+20}_{-20}	$0.005^{+0.002}_{-0.001}$	$0.025^{+0.005}_{-0.004}$	$1.7^{+0.3}_{-0.3}$	≥ 2	$1.1^{+0.3}_{-0.1}$	$0.8^{+0.2}_{-0.1}$
2478	55.22	6.29	110^{+6}_{-9}	$0.003^{+0.0004}_{-0.0006}$	$0.023^{+0.002}_{-0.002}$	≤ 0.51	≥ 2	$1.4^{+0.08}_{-0.1}$	$0.8^{+0.1}_{-0.04}$
2479	54.36	6.33	130^{+10}_{-20}	$0.0023^{+0.0005}_{-0.0001}$	$0.025^{+0.003}_{-0.004}$	≥ 1.7	$1.7^{+0.3}_{-0.3}$	$0.8^{+0.3}_{-0.1}$	$0.8^{+0.3}_{-0.1}$
2480	54.19	6.36	150^{+10}_{-20}	$0.0026^{+0.0004}_{-0.0001}$	$0.028^{+0.003}_{-0.004}$	≤ 0.44	$1.4^{+0.3}_{-0.3}$	$1.7^{+0.09}_{-0.2}$	$0.8^{+0.1}_{-0.1}$
2481	54.24	6.43	130^{+6}_{-5}	$0.0035^{+0.0005}_{-0.0004}$	$0.026^{+0.002}_{-0.001}$	≤ 0.4	$2^{+0.2}_{-0.2}$	$1.4^{+0.09}_{-0.07}$	$0.8^{+0.08}_{-0.07}$
2482	54.08	6.51	150^{+6}_{-6}	$0.0039^{+0.0006}_{-0.0005}$	$0.03^{+0.002}_{-0.001}$	$0.8^{+0.2}_{-0.2}$	$1.4^{+0.2}_{-0.3}$	$1.4^{+0.09}_{-0.08}$	$0.8^{+0.06}_{-0.08}$
2483	53.42	6.64	170^{+9}_{-20}	$0.0044^{+0.0009}_{-0.0001}$	$0.033^{+0.002}_{-0.004}$	$1.7^{+0.3}_{-0.3}$	≤ 0.46	$1.4^{+0.1}_{-0.2}$	$0.8^{+0.07}_{-0.1}$
2484	52.55	6.72	150^{+20}_{-4}	$0.006^{+0.002}_{-0.0006}$	$0.031^{+0.004}_{-0.002}$	≥ 1.8	$1.1^{+0.2}_{-0.1}$	$1.1^{+0.2}_{-0.06}$	$0.8^{+0.08}_{-0.1}$
2485	51.26	6.67	150^{+10}_{-5}	$0.006^{+0.002}_{-0.0005}$	$0.031^{+0.003}_{-0.001}$	≥ 1.8	$1.4^{+0.3}_{-0.2}$	$1.1^{+0.06}_{-0.06}$	$0.8^{+0.06}_{-0.09}$
2486	50.12	6.66	150^{+8}_{-5}	$0.006^{+0.001}_{-0.0006}$	$0.031^{+0.002}_{-0.001}$	≥ 1.7	$1.4^{+0.3}_{-0.3}$	$1.1^{+0.1}_{-0.07}$	$0.8^{+0.06}_{-0.06}$
2487	49.89	6.60	170^{+9}_{-10}	$0.0044^{+0.0005}_{-0.0002}$	$0.033^{+0.002}_{-0.004}$	≤ 0.36	≤ 0.5	$1.4^{+0.07}_{-0.1}$	$0.8^{+0.07}_{-0.1}$
2488	49.67	6.56	170^{+8}_{-7}	$0.007^{+0.001}_{-0.001}$	$0.036^{+0.002}_{-0.002}$	$1.7^{+0.2}_{-0.2}$	≤ 0.48	$1.1^{+0.1}_{-0.1}$	$0.8^{+0.05}_{-0.1}$
2489	49.34	6.52	190^{+9}_{-10}	$0.005^{+0.0005}_{-0.0002}$	$0.038^{+0.002}_{-0.004}$	≤ 0.35	≤ 0.46	$1.4^{+0.06}_{-0.3}$	$0.8^{+0.07}_{-0.1}$
2490	49.14	6.50	190^{+8}_{-8}	$0.008^{+0.002}_{-0.001}$	$0.041^{+0.004}_{-0.004}$	$1.7^{+0.2}_{-0.2}$	≤ 0.5	$1.1^{+0.2}_{-0.1}$	$0.8^{+0.06}_{-0.2}$
2491	48.94	6.47	190^{+20}_{-10}	$0.008^{+0.003}_{-0.002}$	$0.041^{+0.005}_{-0.006}$	$1.4^{+0.3}_{-0.2}$	≤ 0.46	$1.1^{+0.3}_{-0.3}$	$0.8^{+0.06}_{-0.3}$
2492	48.80	6.44	210^{+9}_{-20}	$0.006^{+0.001}_{-0.002}$	$0.038^{+0.005}_{-0.004}$	$0.5^{+0.2}_{-0.2}$	≥ 2	$1.4^{+0.1}_{-0.3}$	$0.50^{+0.3}_{-0.05}$
2493	48.59	6.47	190^{+20}_{-10}	$0.008^{+0.003}_{-0.003}$	$0.041^{+0.005}_{-0.006}$	$1.1^{+0.3}_{-0.2}$	≤ 0.48	$1.1^{+0.3}_{-0.2}$	$0.8^{+0.06}_{-0.3}$
2494	47.84	6.40	210^{+10}_{-10}	$0.009^{+0.003}_{-0.002}$	$0.041^{+0.005}_{-0.003}$	$1.7^{+0.2}_{-0.3}$	≥ 2.1	$1.1^{+0.2}_{-0.1}$	$0.50^{+0.2}_{-0.04}$
2495	47.01	6.37	210^{+9}_{-20}	$0.0056^{+0.0007}_{-0.0002}$	$0.038^{+0.005}_{-0.004}$	≤ 0.36	≥ 2.1	$1.4^{+0.08}_{-0.3}$	$0.50^{+0.3}_{-0.04}$
2496	46.45	6.33	210^{+9}_{-20}	$0.0056^{+0.0007}_{-0.0002}$	$0.038^{+0.005}_{-0.004}$	≤ 0.36	≥ 2.1	$1.4^{+0.08}_{-0.3}$	$0.50^{+0.3}_{-0.04}$
2497	45.86	6.30	210^{+10}_{-20}	$0.009^{+0.002}_{-0.002}$	$0.041^{+0.005}_{-0.004}$	$1.7^{+0.2}_{-0.3}$	≥ 2.1	$1.1^{+0.2}_{-0.2}$	$0.50^{+0.2}_{-0.04}$
2498	45.47	6.20	210^{+10}_{-10}	$0.009^{+0.002}_{-0.003}$	$0.042^{+0.005}_{-0.004}$	$1.4^{+0.2}_{-0.2}$	≥ 2.1	$1.1^{+0.2}_{-0.2}$	$0.50^{+0.2}_{-0.04}$
2499	45.05	6.15	190^{+20}_{-8}	$0.013^{+0.006}_{-0.002}$	$0.046^{+0.006}_{-0.006}$	≥ 1.7	$0.5^{+0.3}_{-0.3}$	$0.8^{+0.3}_{-0.09}$	$0.8^{+0.08}_{-0.3}$
2500	44.38	6.12	230^{+10}_{-20}	$0.01^{+0.003}_{-0.005}$	$0.047^{+0.006}_{-0.005}$	$1.4^{+0.2}_{-0.3}$	$2^{+0.3}_{-0.2}$	$1.1^{+0.2}_{-0.3}$	$0.50^{+0.2}_{-0.05}$
2501	43.52	6.04	210^{+20}_{-20}	$0.014^{+0.006}_{-0.003}$	$0.046^{+0.007}_{-0.004}$	≥ 1.8	≥ 2	$0.8^{+0.3}_{-0.1}$	$0.50^{+0.2}_{-0.05}$
2502	42.56	5.92	210^{+20}_{-20}	$0.015^{+0.006}_{-0.004}$	$0.047^{+0.007}_{-0.005}$	≥ 1.7	≥ 2	$0.8^{+0.3}_{-0.2}$	$0.50^{+0.3}_{-0.05}$
2503	41.26	5.80	210^{+10}_{-20}	$0.015^{+0.006}_{-0.003}$	$0.048^{+0.006}_{-0.004}$	≥ 1.8	≥ 2.1	$0.8^{+0.3}_{-0.1}$	$0.50^{+0.2}_{-0.04}$
2504	39.91	5.67	210^{+10}_{-20}	$0.01^{+0.003}_{-0.004}$	$0.046^{+0.006}_{-0.005}$	$0.5^{+0.2}_{-0.2}$	≥ 2.1	$1.1^{+0.2}_{-0.3}$	$0.50^{+0.2}_{-0.05}$
2505	38.61	5.59	210^{+10}_{-20}	$0.01^{+0.002}_{-0.004}$	$0.047^{+0.006}_{-0.005}$	$0.8^{+0.2}_{-0.2}$	≥ 2.1	$1.1^{+0.1}_{-0.3}$	$0.50^{+0.3}_{-0.05}$
2506	37.77	5.52	170^{+20}_{-20}	$0.013^{+0.005}_{-0.005}$	$0.046^{+0.006}_{-0.007}$	$1.1^{+0.3}_{-0.2}$	$0.5^{+0.3}_{-0.3}$	$0.8^{+0.3}_{-0.3}$	$0.8^{+0.1}_{-0.3}$

Note. See Table 2 for the description of the columns.

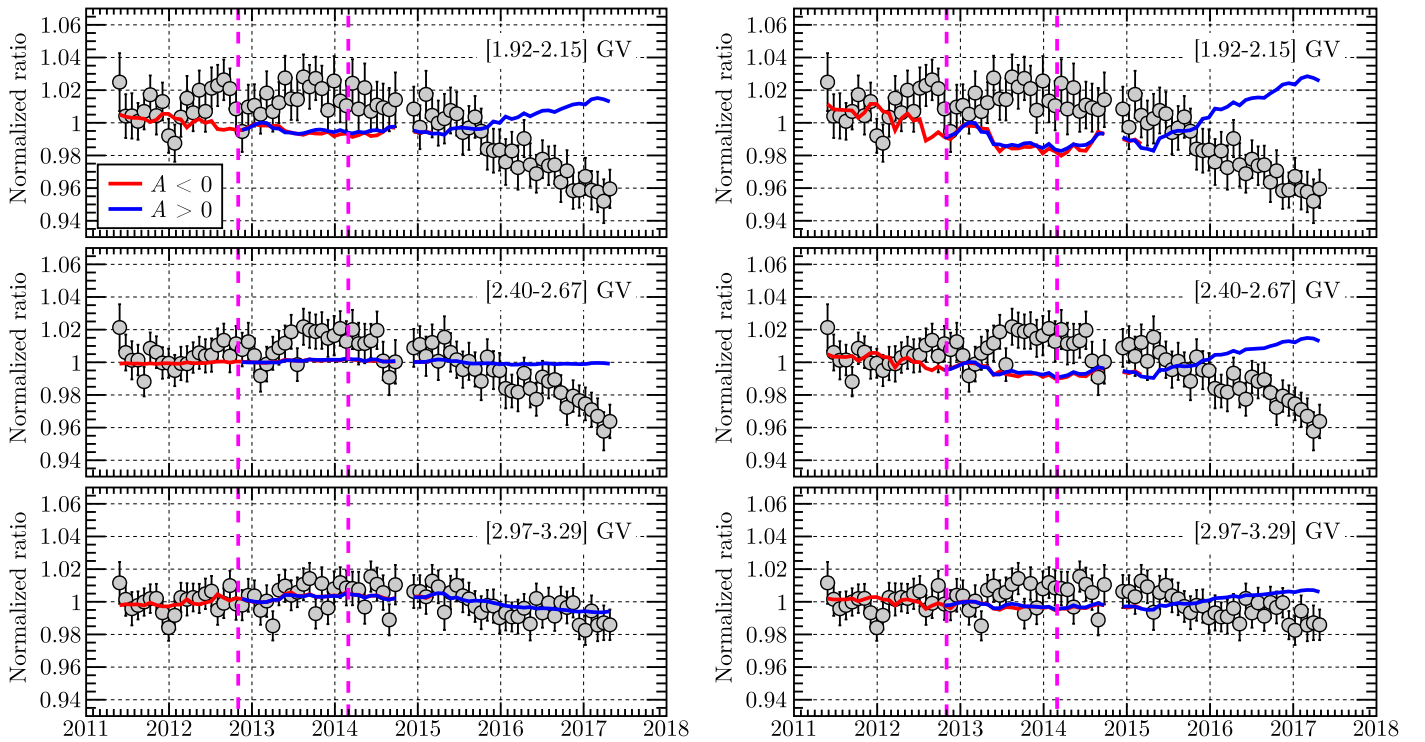


Figure 7. Effect of the difference in LIS shape on the time variation of p/He. The normalized modeled $p/{}^3\text{He}$ (red and blue lines; left) and $p/{}^4\text{He}$ (red and blue lines; right) compared to the observed p/He (gray circles) are shown as a function of time for three selected rigidity bins. The vertical dashed magenta lines delimit the period of the solar magnetic field polarity reversal.

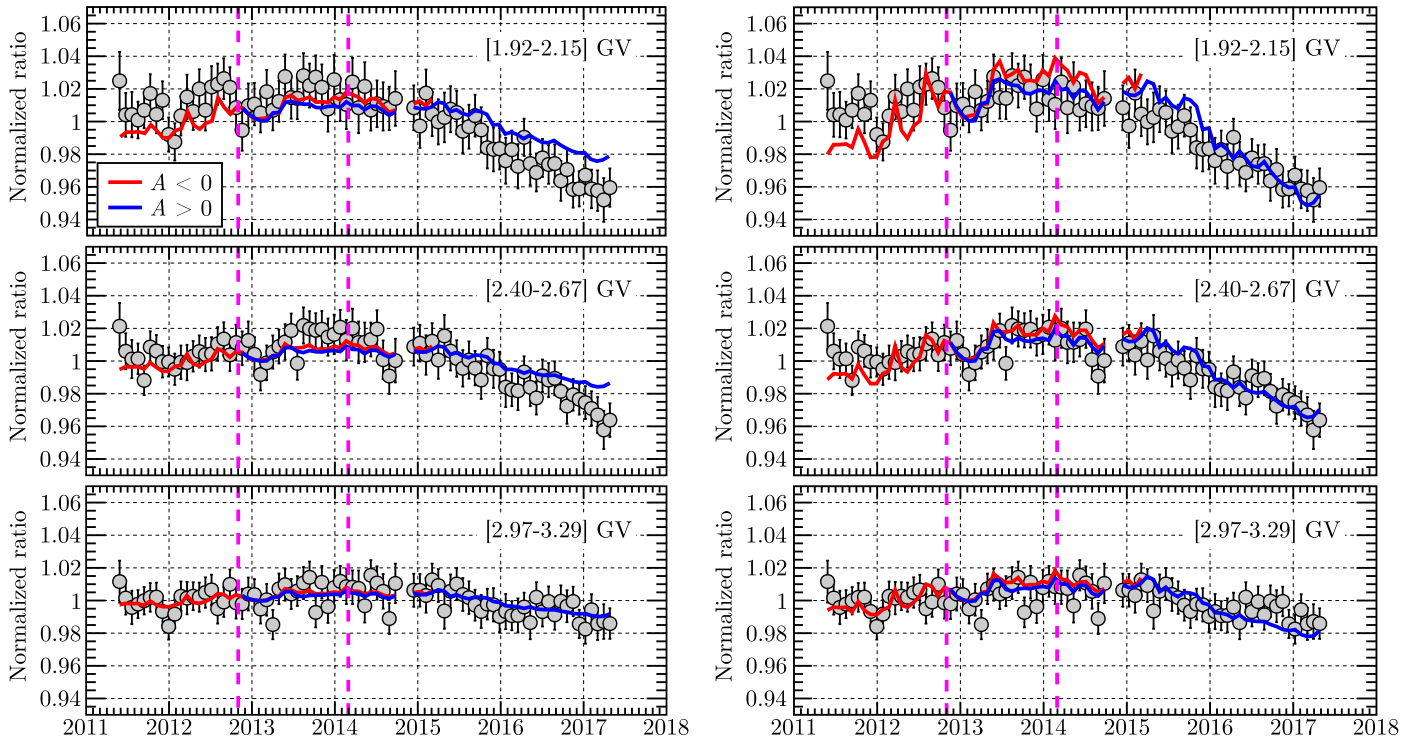


Figure 8. Effect of the A/Z dependence of the diffusion tensor on the time variation of p/He. The normalized modeled $p/{}^3\text{He}$ (red and blue lines; left) and $p/{}^4\text{He}$ (red and blue lines; right) compared to the observed p/He (gray circles) are shown as a function of time for three selected rigidity bins. The vertical dashed magenta lines delimit the period of the solar magnetic field polarity reversal.

p/He behavior is dominated by $p/{}^4\text{He}$; thus, even taking into account the uncertainty on the ${}^3\text{He}$ and ${}^4\text{He}$ LISs, the observed p/He can not be reproduced if we assume the same A/Z but different LIS.

The relation between the time variation and the spectral index could be tested with a long-term measurement of the ratio of two species with exactly the same A/Z , for example, deuterons and ${}^4\text{He}$. Because of its large acceptance and

precision, AMS-02 might be able to perform such a measurement.

6.2. Charge-to-mass Ratio Dependence of the Diffusion Tensor

To understand the effect of the A/Z dependence of the diffusion tensor, we ran the best-fit models for p, ${}^3\text{He}$, and ${}^4\text{He}$, forcing the same LIS for all three species but using the appropriate A/Z for each particle. In the following, p corresponds to the proton LIS and $A/Z = 1$, ${}^3\text{He}$ corresponds to the proton LIS and $A/Z = 3/2$, while ${}^4\text{He}$ corresponds to the proton LIS and $A/Z = 2$.

Figure 8 shows the comparison of the normalized modeled $p/{}^3\text{He}$ (red and blue lines; left panels) and $p/{}^4\text{He}$ (red and blue lines; right panels) with the normalized observed p/He (gray circles) for the same rigidity bins as in Figure 7.

The time trend of the observed p/He is reproduced, but for ${}^3\text{He}$ models, the amplitude of the decrease below 3 GV is smaller than that for the data and ${}^4\text{He}$ models; the difference in A/Z between ${}^3\text{He}$ and ${}^4\text{He}$ is clearly playing an important role.

It is interesting to consider the ratio between particle velocities: at 2 GV, $v(p)/v({}^3\text{He}) = 1.1$, while $v(p)/v({}^4\text{He}) = 1.23$; at 2.5 GV, $v(p)/v({}^3\text{He}) = 1.07$, while $v(p)/v({}^4\text{He}) = 1.16$; and at 3 GV, $v(p)/v({}^3\text{He}) = 1.05$, while $v(p)/v({}^4\text{He}) = 1.12$. The values of $v(p)/v({}^3\text{He})$ at 2 GV and $v(p)/v({}^4\text{He})$ at 3 GV are very similar, and so is the amplitude of the decrease of $p/{}^3\text{He}$ at 2 GV and $p/{}^4\text{He}$ at 3 GV. This suggests that the magnitude of the time variation of the ratio of two species with the same LIS is proportional to the velocity ratio of the two species. As seen in Section 4, k_{\parallel}^0 is the main parameter that determines the level of modulation of the flux, so it is reasonable to expect that the amplitude of the variation of p/He depends on the component-wise ratio $K(p)/K(\text{He}) = v(p)/v(\text{He})l$.

These results do not depend on the choice of the LIS. Using any parameterization of the ${}^3\text{He}$ or ${}^4\text{He}$ LISs, we obtain the same normalized $p/{}^3\text{He}$ and $p/{}^4\text{He}$ as the results presented in Figure 8.

The two tests show that the observed p/He time variation is most probably due to the A/Z dependence of the diffusion tensor, since the difference in LIS shape should produce the opposite time behavior between 2 and 3 GV. However, PAMELA was able to measure p/He at lower rigidities than AMS-02 (down to 0.4 GV) and took measurements at different solar activity conditions (from the minimum of solar cycle 23/24 to the maximum of solar cycle 24). At 1 GV, the spectral index of the $p/{}^3\text{He}$ and $p/{}^4\text{He}$ LIS ratios is negative and greater (in absolute value) than that at 2 GV, so it might be possible that the difference in LIS shape plays a bigger role at 1 GV than at 2 GV.

As noted before, the symmetric components of \mathbf{K} depend on A/Z , but the diffusion tensor also contains the drift coefficient, k_A , in its antisymmetric part. From Equation (12), we see that k_A is a function of A/Z , so we might expect a different behavior of the time dependence of p/He according to the HMF polarity. We verified that this is not the case by repeating the tests with best-fit models with both polarities for all BRs. The difference between the $A < 0$ and $A > 0$ models is of the order of 0.5% for $R \geq 2$ GV. The drift effects for protons become larger below 1 GV (Potgieter & Vos 2017), so the PAMELA data might be able to reveal a difference in the time variation of p/He before and after the polarity reversal, due to the A/Z dependence of the drift coefficient.

7. Conclusions

Understanding diffusion processes in the heliosphere is crucial to improving predictions of the time variation of GCR fluxes at Earth and other locations of interest. The recently published monthly proton and helium fluxes measured by AMS-02 allow the detailed study of the effects of solar modulation during the ascending phase, solar maximum, and descending phase of solar cycle 24. It was observed by AMS-02 that the proton flux at 1 and 5 GV behaves differently with time during the period of the solar maximum: the flux intensity at 1 GV keeps decreasing until the peak of solar activity, while at 5 GV, it remains flatter. Instead, the AMS-02 p/He ratio below 3 GV is constant in time until 2015 March; then it starts to decrease, at the same time that proton and helium fluxes start to recover, while the solar cycle progresses toward the next minimum.

In this work, a sophisticated state-of-the-art 3D numerical model has been tuned to reproduce the monthly proton fluxes measured by AMS-02. The fitted normalization of the parallel diffusion coefficient is well correlated with the proton flux intensity at 5 GV and anticorrelated with the sunspot number. The different time behavior of the proton flux at 1 and 5 GV is determined by the slope of the perpendicular diffusion coefficient. During the period of maximum solar activity, the perpendicular mean free path decreases more at low rigidities than at high rigidities.

Assuming the same mean free path for p, ${}^3\text{He}$ and ${}^4\text{He}$, the best-fit models are able to reproduce the observed time trend of the p/He ratio, albeit with a small rigidity-dependent normalization shift, most probably due to a bias in the ${}^3\text{He}$ and ${}^4\text{He}$ LIS parameterization.








To understand the origin of the time dependence of p/He , two separate tests were performed. First, the model was run assuming a different LIS for p, ${}^3\text{He}$, and ${}^4\text{He}$ but the same mass-to-charge ratio, A/Z , to explore how the difference in LIS shape can affect the time variation of p/He . Then, the model was run assuming the same LIS for p, ${}^3\text{He}$, and ${}^4\text{He}$ but a different A/Z , to check the effect of the A/Z dependence of the diffusion tensor. The second test was able to reproduce the observed p/He time variation, while the first test was not. Thus, the A/Z dependence of the diffusion tensor seems to be the dominant cause of the time variation of p/He , at least in the rigidity range between 2 and 3 GV. Data from PAMELA on p/He at lower rigidities and from AMS-02 on $d/{}^4\text{He}$ would shed light on the importance of the difference in the LIS shape.

We would like to thank E. E. Vos, R. D. Strauss, N. Tomassetti, and S. Della Torre for fruitful discussions about the physics of GCR transport in the heliosphere. We acknowledge the financial support of National Science Foundation Early Career under grant NSF AGS-1455202; Wyle Laboratories, Inc., under grant NAS 9-02078; and NASA under grant 17-SDMSS17-0012. M.S.P. acknowledges the financial support of the South African National Research Foundation (NRF) under the Competitive Funding for Rated Researchers grant 68198.

Note added. While this work was in review, we became aware of a related study from Tomassetti et al. (2018). Their work is based on the same data sets as ours, but it follows different approaches for the

galactic and heliospheric transport modeling. Their results are consistent with those presented in this manuscript.

ORCID iDs

Claudio Corti  <https://orcid.org/0000-0001-9127-7133>
 Marius S. Potgieter  <https://orcid.org/0000-0003-0793-7333>
 Veronica Bindi  <https://orcid.org/0000-0002-6706-0556>
 Cristina Consolandi  <https://orcid.org/0000-0003-4257-4187>
 Christopher Light  <https://orcid.org/0000-0002-8403-2004>
 Matteo Palermo  <https://orcid.org/0000-0002-0135-8181>
 Alexis Popkow  <https://orcid.org/0000-0002-3157-8839>

References

- Accardo, L., Aguilar, M., Aisa, D., et al. 2014, *PhRvL*, **113**, 121101
 Adriani, O., Barbarino, G. C., Bazilevskaya, G. A., et al. 2010, *PhRvL*, **105**, 121101
 Adriani, O., Barbarino, G. C., Bazilevskaya, G. A., et al. 2013a, *PhRvL*, **111**, 81102
 Adriani, O., Barbarino, G. C., Bazilevskaya, G. A., et al. 2013b, *ApJ*, **765**, 91
 Adriani, O., Barbarino, G. C., Bazilevskaya, G. A., et al. 2016, *ApJ*, **818**, 68
 Aguilar, M., Aisa, D., Alpat, B., et al. 2015, *PhRvL*, **114**, 171103
 Aguilar, M., Alcaraz, J., Allaby, J., et al. 2011, *ApJ*, **736**, 105
 Aguilar, M., Ali Cavasonza, L., Ambrosi, G., et al. 2016b, *PhRvL*, **117**, 231102
 Aguilar, M., Ali Cavasonza, L., Ambrosi, G., et al. 2017, *PhRvL*, **119**, 251101
 Aguilar, M., Ali Cavasonza, L., Alpat, B., et al. 2016a, *PhRvL*, **117**, 091103
 Aguilar, M., Ali Cavasonza, L., Alpat, B., et al. 2018, *PhRvL*, **121**, 051101
 Amato, E., & Blasi, P. 2017, *AdSpR*, **62**, 0273
 Bieber, J. W., Matthaeus, W. H., Shalchi, A., & Qin, G. 2004, *GeoRL*, **31**, L10805
 Bisschoff, D., & Potgieter, M. S. 2016, *Ap&SS*, **361**, 48
 Blasi, P., & Serpico, P. D. 2009, *PhRvL*, **103**, 081103
 Blum, K., Katz, B., & Waxman, E. 2013, *PhRvL*, **111**, 211101
 Burger, R. A., Potgieter, M. S., & Heber, B. 2000, *JGRA*, **105**, 27447
 Cirelli, M., Gaggero, D., Giesen, G., Taoso, M., & Urbano, A. 2014, *JCAP*, **2014**, 045
 Corti, C., Bindi, V., Consolandi, C., & Whitman, K. 2016, *ApJ*, **829**, 8
 Cucinotta, F. A., & Durante, M. 2006, *The Lancet Oncology*, **7**, 431
 Cucinotta, F. A., Kim, M. Y., & Chappell, L. J. 2013, Space Radiation Cancer Risk Projections and Uncertainties, NASA Tech. Paper 2013-217375 (Washington, DC: NASA)
 Cummings, A. C., Stone, E. C., Heikkila, B. C., et al. 2016, *ApJ*, **831**, 18
 Donato, F., Maurin, D., Brun, P., Delahaye, T., & Salati, P. 2009, *PhRvL*, **102**, 071301
 Fornengo, N., Maccione, L., & Vittino, A. 2013, *JCAP*, **2013**, 031
 Fornengo, N., Maccione, L., & Vittino, A. 2014, *JCAP*, **2014**, 003
 Gleeson, L. J., & Axford, W. I. 1968, *ApJ*, **154**, 1011
 Heber, B., & Potgieter, M. S. 2006, *SSRv*, **127**, 117
 Hoeksema, J. T. 1995, *SSRv*, **72**, 137
 Hooper, D., Blasi, P., & Serpico, P. D. 2009, *JCAP*, **2009**, 025
 James, F., & Roos, M. 1975, *CoPhC*, **10**, 343
 Kolmogorov, A. N. 1941, *DoSSR*, **30**, 301
 Kopp, A., Wiengarten, T., Fichtner, H., et al. 2017, *ApJ*, **837**, 37
 Kóta, J., & Jokipii, J. R. 1983, *ApJ*, **265**, 573
 Kóta, J., & Jokipii, J. R. 1995, *ICRC*, **4**, 680
 Langner, U. W., & Potgieter, M. S. 2005, *AdSpR*, **35**, 2084
 Luo, X., Potgieter, M. S., Zhang, M., & Feng, X. 2017, *ApJ*, **839**, 53
 Martucci, M., Munini, R., Boezio, M., et al. 2018, *ApJL*, **854**, L2
 Maurin, D., Melot, F., & Taillet, R. 2014, *A&A*, **569**, 32
 Myers, Z. D., Seo, E. S., Abe, K., et al. 2003, *ICRC*, **4**, 1805
 Ngobeni, M. D., & Potgieter, M. S. 2014, *AdSpR*, **53**, 1634
 Ngobeni, M. D., & Potgieter, M. S. 2015, *AdSpR*, **56**, 1525
 Nndanganeni, R. R., & Potgieter, M. S. 2016, *AdSpR*, **58**, 453
 Parker, E. N. 1958, *ApJ*, **128**, 664
 Parker, E. N. 1965, *P&SS*, **13**, 9
 Peaceman, D. W., & Rachford, H. H., Jr. 1955, *J. Soc. Ind. Appl. Math.*, **3**, 28
 Potgieter, M. S. 2014, *BrJPh*, **44**, 581
 Potgieter, M. S. 2000, *JGRA*, **105**, 18295
 Potgieter, M. S. 2013a, *LRSV*, **10**, 3
 Potgieter, M. S. 2013b, *SSRv*, **176**, 165
 Potgieter, M. S. 2017, *AdSpR*, **60**, 848
 Potgieter, M. S., & Haasbroek, L. J. 1993, *ICRC*, **3**, 457
 Potgieter, M. S., & Vos, E. E. 2017, *A&A*, **601**, A23
 Potgieter, M. S., Vos, E. E., Boezio, M., et al. 2014, *SoPh*, **289**, 391
 Raath, J. L., Potgieter, M. S., Strauss, R. D., & Kopp, A. 2016, *AdSpR*, **57**, 1965
 Raath, J. L., Strauss, R. D., & Potgieter, M. S. 2015, *Ap&SS*, **360**, 56
 Reimer, O., Menn, W., Hof, M., et al. 1998, *ApJ*, **496**, 490
 SILSO World Data Center 2011, Royal Observatory of Belgium, Brussels, International Sunspot Number Monthly Bulletin and Online Catalog, <http://www.sidc.be/silso/>
 Smith, C. W., & Bieber, J. W. 1991, *ApJ*, **370**, 435
 Stone, E. C., Cummings, A. C., McDonald, F. B., et al. 2013, *Sci*, **341**, 150
 Strauss, R. D., Potgieter, M. S., Kopp, A., & Büsching, I. 2011, *JGRA*, **116**, 12105
 Tomassetti, N. 2017, *PhRvD*, **96**, 103005
 Tomassetti, N., Barão, F., Bertucci, B., et al. 2018, *PhRvL*, **121**, 251104
 Tomassetti, N., Orcinha, M., Barão, F., & Bertucci, B. 2017, *ApJL*, **849**, L32
 Turner, M. S., & Wilczek, F. 1990, *PhRvD*, **42**, 1001
 Vos, E. E., & Potgieter, M. S. 2015, *ApJ*, **815**, 119
 Wang, J., Seo, E. S., Anraku, K., et al. 2002, *ApJ*, **564**, 244
 Webber, W. R., Lal, N., & Heikkila, B. C. 2018, arXiv:1802.08273
 Webber, W. R., McDonald, F. B., Cummings, A. C., et al. 2012, *GeoRL*, **39**, L06107
 Yuan, Q., & Bi, X.-J. 2015, *JCAP*, **2015**, 033
 Zhao, L.-L., Qin, G., Zhang, M., & Heber, B. 2014, *JGRA*, **119**, 1493